

Two-particle correlations at small relative momenta for ^{40}Ar -induced reactions on ^{197}Au at $E/A=60$ MeV

J. Pochodzalla,* C. K. Gelbke, W. G. Lynch, and M. Maier

National Superconducting Cyclotron Laboratory, Michigan State University, East Lansing, Michigan 48824

D. Ardouin,[†] H. Delagrange, H. Doubre, C. Grégoire, A. Kyanowski,[‡] W. Mittig,
A. Péghaire, J. Péter, F. Saint-Laurent, and B. Zwieglinski[§]

Laboratoire GANIL, 14021 Caen Cedex, France

G. Bizard, F. Lefèbvres, and B. Tamain

Laboratoire de Physique Corpusculaire, Université de Caen, 14032 Caen Cedex, France

J. Québert

Centre d'Etudes Nucléaires de Bordeaux, 33170 Gradignan, France

Y. P. Viyogi

*Variable Energy Cyclotron Centre, Calcutta 700064, India
and Laboratoire GANIL, 14021 Caen Cedex, France*

W. A. Friedman

Department of Physics, University of Wisconsin, Madison, Wisconsin 53706

D. H. Boal

Department of Physics, Simon Fraser University, Burnaby, British Columbia, Canada V5A1S6

(Received 4 September 1986)

Two-particle correlations at small relative momenta provide information about the space-time extent and the excitation energy density of the emitting system. Detailed measurements of two-particle correlations were performed for ^{40}Ar -induced reactions on ^{197}Au at $E/A=60$ MeV. In general, more pronounced correlations are measured for particles of higher outgoing energy. From the relative populations of excited states, a mean emission temperature of $T \approx 5.5$ MeV is extracted. Within the framework of the quantum statistical model, our findings are consistent with an expanding nuclear system which disintegrates at low temperature ($T \approx 5.5$ MeV) and rather low density ($\rho \leq 0.1\rho_0$).

I. INTRODUCTION

The formation and decay of highly excited nuclear systems in intermediate energy nucleus-nucleus collisions ($E/A \approx 20\text{--}200$ MeV) presents a challenging problem. At these energies, the nuclear mean field as well as individual nucleon-nucleon collisions are important for a quantitative understanding of the reaction dynamics.¹⁻⁴ Although a detailed dynamical description of the spatial and temporal evolution of the collision process is still beyond reach, significant progress has been made by the application of quasistatic statistical concepts. Several approaches are based on the assumption of local statistical equilibrium and describe the system in terms of a few state variables, e.g., temperature, entropy, and density.⁵⁻¹⁰ Such approaches may not be accurate because of the finite spatial size and the finite lifetime of the reaction zone.¹¹ Additional complication can arise due to constraints imposed by conservation laws, fluctuations,¹²⁻¹⁴ quantum mechanical binding, and long range Coulomb effects.^{15,16} It is clearly important to perform experiments which test the

validity of statistical concepts and which are sensitive to the space-time evolution of the reaction.

Most attempts to obtain experimental information about the temperature of highly excited nuclear systems were based on analyses of the kinetic energy spectra of the emitted particles.¹⁷ For ^{40}Ar induced reactions on ^{197}Au , the energy spectra of particles emitted at midrapidities could be rather well described¹⁸ in terms of simple Maxwellian distributions, characterized by temperature parameters which were nearly independent of the emitted fragments. This observation is consistent with the assumption that the velocity distributions of the particles are close to the equilibrium limit. However, the interpretation of the kinetic energy spectra is complicated by their sensitivity to the collective motion,^{19,20} the temporal evolution of the emitting system,^{8,9,21,22} the sequential decay of highly excited primary fragments,^{8,22} and fluctuations of the Coulomb barrier.¹³

An alternative determination of the temperature at the point at which the particles leave the equilibrated (sub)system is based on the relative population of states.

This approach is meaningful if the emitting subsystem is not only close to kinetic equilibrium but also close to chemical equilibrium. If the phase space of the decay configuration is known, this “emission temperature” can be determined from the relative abundances of different particle species^{23–25} or—more directly and less model dependent—from the relative populations of states in a given nucleus.^{26–29} Since feeding from higher lying particle unbound states^{6,30–34} and neutron induced deexcitations³⁵ can alter the primary populations, these temperature measurements can be associated with large uncertainties whenever the level separations are smaller than the emission temperatures.^{27,36}

Because of their sensitivity to quantum statistics^{37–39} and final-state interactions,^{40–42} two-particle correlation functions at small relative momenta contain information about the space-time characteristics of the emitting system. For intermediate energy nucleus-nucleus collisions, two proton,^{43–45} two-deuteron,^{45,46} two-triton,^{45,46} proton-alpha,⁴⁵ and deuteron-alpha^{45,47,48} correlation functions have been used to explore the space-time evolution of the emitting system. The interpretation of two-particle correlations can, however, be complicated by additional sensitivities to ensemble averaging,⁴⁹ reaction dynamics,⁵⁰ momentum conservation,⁴³ Coulomb distortions,^{51,52} and higher order decays.⁵² Since correlations between different particles are expected to exhibit different sensitivities to these effects, the measurement of two-particle correlations for several light-particle combinations in a given reaction may provide a unique tool with which one can study these effects and obtain detailed information about the spatial and temporal evolution of the emitting system.^{35,46,47,53}

In order to obtain more detailed information about emission temperatures, sequential decay processes, and the space-time evolution of the reaction, we have measured two-particle correlation functions at small relative momenta for ⁴⁰Ar induced reactions on ¹⁹⁷Au at $E/A=60$ MeV. Some of our results have been reported previously.^{27,29,52} The paper is organized as follows. Experimental details will be given in the following section. In Sec.

III single particle inclusive cross sections will be presented. Two-particle correlation functions will be presented in Sec. IV. Source radii will be extracted and their energy dependence will be discussed. Distortions of two-particle correlation functions by the influence of a third unobserved particle will be discussed. In Sec. V the relative populations of particle unbound states will be investigated and emission temperatures will be extracted. The importance of sequential feeding from the decay of particle unbound primary fragments is quantified in Sec. VI. A summary is given in Sec. VII.

II. EXPERIMENTAL DETAILS

The experiment was performed at the Laboratoire Grand Accélérateur National d'Ions Lourds (GANIL) at Caen. A gold target of 10 mg/cm² areal density was irradiated by a ⁴⁰Ar beam of $E/A=60$ MeV incident energy. The size of the beam spot on target was approximately 1×2 mm². Light particles ($Z \leq 3$) were detected by a close-packed hexagonal array of thirteen ΔE - E telescopes, each consisting of a 400 μ m thick silicon detector and a 10 cm thick NaI(Tl) scintillator. With these telescopes, all particles between protons and ⁷Li were separated. The detectors were located at a distance of 61 cm from the target; the center of the hodoscope was positioned at a laboratory angle of $\theta_{av}=30^\circ$. The angular separation between adjacent telescopes was $\Delta\theta=4.2^\circ$; the maximum relative angle was 14.6° . Each telescope subtended a solid angle of 0.46 msr corresponding to a resolution of the relative angle of $\delta(\Delta\theta)_{FWHM} \approx 1.2^\circ$ (where FWHM denotes full width at half maximum). Similar ΔE - E telescopes, positioned at laboratory angles of $30^\circ, 70^\circ, 110^\circ, 135^\circ,$ and 160° , were used to measure the single particle inclusive cross sections. In-plane and out-of-plane two-particle correlations at large relative momenta were measured by varying the azimuthal angle of some of those telescopes between 35° and 180° . In addition, coincident light particles were detected in a multidetector array⁵⁴ which covered an angular range of 3° – 30° . A schematic drawing of the setup is shown in Fig. 1. In this paper we will present two-

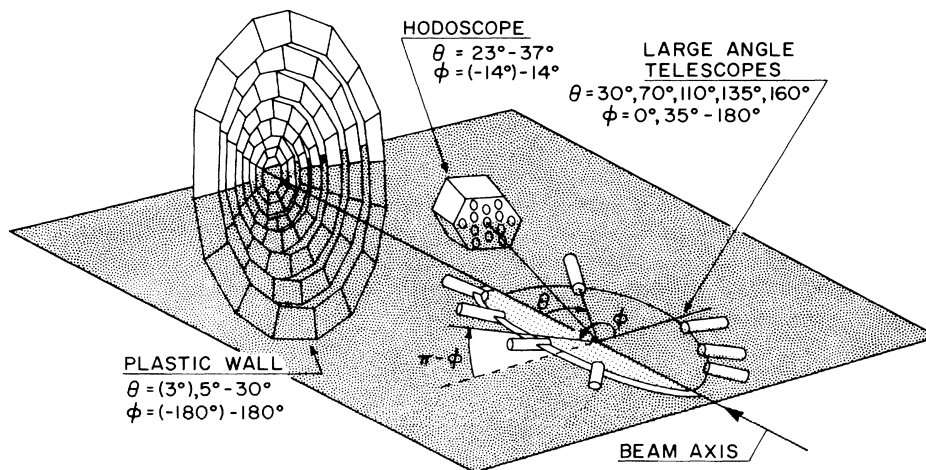


FIG. 1. Schematic view of the experimental setup.

particle correlations at small relative momenta, measured with the 13-element hodoscope, and inclusive cross sections measured with the large angle telescopes. Two-particle correlations at large relative momenta and the effects of event selection with the forward angle multidetector array will be presented elsewhere.^{55,56}

Energy calibrations and energy resolutions were established by bombarding a thick carbon target with ^{40}Ar ions, and analyzing the reaction products according to their magnetic rigidity with a 270° beam transport system. These particles were then injected into the telescopes. Previous investigations⁵⁷ found that the reduced light output of a scintillator, L/AZ^2 , depends primarily on the reduced energy, E/AZ^2 , where A and Z denote the mass and charge of the detected particle. We have, therefore, adopted the following functional form for our energy calibrations:

$$E/AZ^2 = a_1 + a_2(L/AZ^2) + a_3(L/AZ^2)^2. \quad (1)$$

For each element, the coefficients a_i ($i=1-3$) were adjusted to provide an optimum fit to the calibration points. Since individual detectors exhibited different nonlinearities, each detector had to be calibrated separately. The energy calibration of the silicon detectors was obtained by injecting a known amount of charge at the detector side of the preamplifier. The overall energy calibrations are accurate to within 2%. The total energy resolution of the telescopes varied between about 1% and 2.5%.

Gain shifts of the photomultiplier tubes were monitored by a light pulser system. As an alternative control of the gain stability of the NaI detectors, we made use of the high stability of the ΔE silicon detectors. To monitor the gain stability, the raw data were sorted into two-dimensional ΔE - E matrices. Several narrow gates were set on the ΔE axis. Events which fell into these gates were projected onto the E axis. Several peaks, corresponding to different types of particles, were obtained for each gate. Each of these peaks was fitted with a Gaussian

function to determine the peak location, P_i . The relative gain shift with respect to the calibration run was then determined by minimizing the function $f(\xi)$,

$$f(\xi) = \sum_i (\xi P_i - P_{0i})^2 / P_{0i}^2, \quad (2)$$

with respect to the gain shift parameter, ξ . Here, the peak locations determined for the calibration run are denoted by P_{0i} . With these procedures, gain shifts of the order of 1% could be detected and corrected.

Coincidence and down-scaled singles events were written on magnetic tape and analyzed off line. During the experiment, the energy thresholds were set at a value equivalent to about 7 MeV protons. In the off-line analysis, thresholds of 12, 15, 18, 35, 40, 45, 80, and 90 MeV were used for p, d, t, ^3He , ^4He , ^6He , ^6Li , and ^7Li , respectively. The correlation data were corrected for random coincidences. Absolute cross sections were determined from the known detector geometry, target thickness, and the integrated beam current. The uncertainty of the absolute normalization was estimated to be less than 25%.

III. SINGLE PARTICLE INCLUSIVE CROSS SECTIONS

Figure 2 shows the single particle inclusive cross sections for protons, deuterons, tritons, and alpha particles. Consistent with previous measurements at similar energies,¹⁸ the spectra exhibit rather featureless exponential slopes at higher energies which become steeper at larger angles. In the center-of-mass system, the cross sections are peaked at forward angles, indicating emission prior to the establishment of full statistical equilibrium of the composite nuclear system. To bring the data into context with previous measurements^{17,18,58} and to provide reasonable extrapolations to unmeasured scattering angles and particle energies, the data were fitted by a "moving source" parametrization employing the superposition of

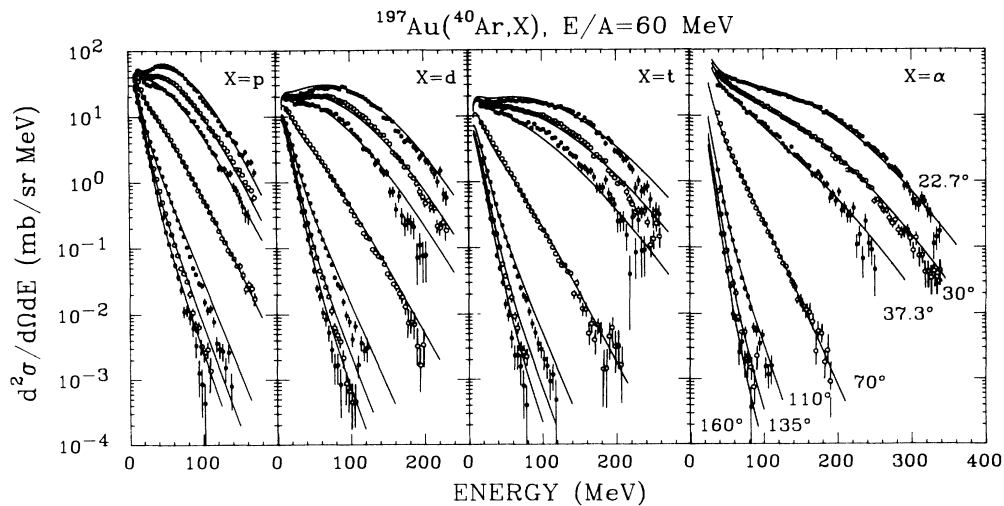


FIG. 2. Differential cross sections for p, d, t, and α particles. The solid lines correspond to fits with Eq. (3).

three Maxwellian distributions:

$$\frac{d^2\sigma}{d\Omega dE} = \sum_{i=1}^3 N_i \sqrt{E - U_C} \times \exp\{-[E - U_C + E_i - 2\sqrt{E_i(E - U_C)}\cos\theta]/T_i\} . \quad (3)$$

Here, U_C is the kinetic energy gained by the Coulomb repulsion from the emitting system, N_i is a normalization constant, and T_i is the “temperature” parameter of the i th source; $E_i = \frac{1}{2}mv_i^2$, where m is the mass of the particle and v_i is the source velocity in the laboratory system. Because of our relatively high energy thresholds, U_C was kept constant at a value of about one-half of the Coulomb barrier for surface emission,^{59,60} see Table I. [For our purposes, the nonrelativistic expression, Eq. (3), is adequate. If one uses the corresponding relativistic expression^{17,58} the extracted temperature parameters change by less than 0.2 MeV and the extracted source velocities change by less than 5%.] In order to obtain a satisfactory description of the energy spectra at backward angles ($\theta > 90^\circ$), it was necessary to introduce a slow source ($v_1 \approx 0.02c$) with a relatively low temperature, $T_1 \approx 6$ MeV.⁶⁰ Contributions of this source at forward angles ($\theta < 50^\circ$) are negligible. For an improvement of the fits to the proton and deuteron distributions at the most forward angles, a fast moving source ($v_3 \approx 0.3c$) was introduced.

Best fits of the three-source parametrization to the data are shown as solid lines in Fig. 2; the parameters are listed in Table I. For tritons and alpha particles fits of similar quality were obtained with two sources. This is expressed in the similarity of the temperature parameter of the fast and intermediate rapidity source listed in Table I. In all cases, the addition of the “projectile-like” source had little influence on the temperature parameter, T_2 , of the intermediate rapidity source [$v_2 \approx (0.11-0.16)c$]. For a two-source fit, the temperature parameters of the intermediate rapidity source are 16.6, 19.2, 19.6, and 14.5 MeV for protons, deuterons, tritons, and alpha particles, respectively. The intermediate rapidity source dominates the energy integrated cross section in the angular range of the hodoscope. The parameters extracted for this source are consistent with the systematic trends established previously:¹⁷ At intermediate rapidities, the kinetic energy spectra can

be characterized by a source of temperature $T_2 \approx 14-18$ MeV and mean velocity of one-third to one-half of the beam velocity.

IV. TWO-PARTICLE CORRELATION FUNCTIONS

A. General considerations

The two-particle correlation function $R(\mathbf{q})$ is defined in terms of the coincidence yield, $Y_{12}(\mathbf{p}_1, \mathbf{p}_2)$, and the single particle yields, $Y_1(\mathbf{p}_1)$ and $Y_2(\mathbf{p}_2)$:

$$\sum Y_{12}(\mathbf{p}_1, \mathbf{p}_2) = C_{12}[1 + R(\mathbf{q})] \sum Y_1(\mathbf{p}_1) \cdot Y_2(\mathbf{p}_2) . \quad (4)$$

Here, \mathbf{p}_1 and \mathbf{p}_2 are the laboratory momenta of the particles 1 and 2; \mathbf{q} is the momentum of relative motion [non-relativistically, \mathbf{q} is given by $\mu(\mathbf{p}_2/m_2 - \mathbf{p}_1/m_1)$]; C_{12} is a normalization constant which is determined by the requirement that $R(q) = 0$ for large relative momenta. For each gating condition, the sums on both sides of Eq. (4) were extended over all energy and detector combinations corresponding to the given bins of \mathbf{q} ; in most cases the correlation functions were determined as a function of $q = |\mathbf{q}|$ only.

Two-particle correlations are sensitive to the space-time extent of the emitting system. This can be understood most easily in the thermal model.⁴² If one assumes that two particles only interact with each other and not with the rest of the system, one may approximate the two-particle density of states as

$$\rho(P, q) = \rho_0(P)\rho(q) . \quad (5)$$

Here, $\rho_0(P) = VP^2/2\pi^2$ denotes the density of states associated with the motion of the center of mass of the two particles, P denotes the total momentum of the two particles, and V denotes the volume of the system. The density of states for the relative motion of the two particles can be approximated as

$$\rho(q) = \rho_0(q) + \Delta\rho(q) . \quad (6)$$

Here, the plane wave density of states for particles with spin s_i ($i = 1, 2$) is given by

$$\rho_0(q) = (2s_1 + 1)(2s_2 + 1) \frac{Vq^2}{2\pi^2} . \quad (7)$$

For nonidentical particles, the interaction term $\Delta\rho$ can be written as⁶¹

TABLE I. Source parameters of three-source fits, Eq. (3), to the single particle inclusive spectra shown in Fig. 2. U_C denotes the Coulomb repulsion; T_i , v_i , and N_i (in mb/sr MeV^{1/2}) are the temperature, velocity, and normalization constant for the i th source, when $i = 1, 2$, and 3 denote the slow, intermediate rapidity, and fast sources, respectively.

| Particle | U_C (MeV) | T_1 (MeV) | v_1 (c) | N_1 | T_2 (MeV) | v_2 (c) | N_2 | T_3 (MeV) | v_3 (c) | N_3 |
|----------|----------------|----------------|--------------|-------|----------------|--------------|-------|----------------|--------------|-------|
| p | 5 | 5.6 | 0.007 | 25.33 | 16.0 | 0.159 | 11.52 | 7.7 | 0.358 | 11.93 |
| d | 5 | 6.7 | 0.018 | 9.52 | 18.0 | 0.150 | 5.11 | 10.5 | 0.314 | 6.96 |
| t | 5 | 6.9 | 0.026 | 7.68 | 17.0 | 0.124 | 3.20 | 14.7 | 0.259 | 3.34 |
| α | 10 | 6.1 | 0.028 | 57.79 | 14.1 | 0.109 | 8.40 | 13.5 | 0.249 | 6.13 |

$$\Delta\rho(q) = \frac{1}{\pi} \sum_{J,\alpha} (2J+1) \frac{\partial\delta_{J,\alpha}}{\partial q}. \quad (8)$$

Here, J is the total angular momentum and $\delta_{J,\alpha}$ is the scattering phase shift for channel α . Contrary to the plane-wave densities, the interaction term does not depend on the size of the system. Introducing the plane wave densities of states for particles 1 and 2,

$$\rho_0(p_i) = (2s_i + 1)Vp_i^2/2\pi^2 \quad (i = 1, 2), \quad (9)$$

one obtains

$$\rho(P, q) \approx \rho_0(P)\rho_0(q)[1 + R(q)] = \rho_0(p_1)\rho_0(p_2)[1 + R(q)], \quad (10)$$

where the correlation function is given by

$$R(q) = \frac{2\pi}{(2s_1 + 1)(2s_2 + 1)Vq^2} \sum_{J,\alpha} (2J+1) \frac{\partial\delta_{J,\alpha}}{\partial q}. \quad (11)$$

If one assumes that the singles and coincidence yields are given by the thermal distributions,

$$Y_i(p_i) \propto \rho_0(p_i) e^{-E_i/T} \quad (i = 1, 2) \quad (12)$$

and

$$Y_{12}(p_1, p_2) \propto \rho(P, q) e^{-(E_1 + E_2)/T}, \quad (13)$$

one can see immediately that $R(q)$ agrees with the definition of Eq. (4). Within the thermal model, the two-particle correlation function depends only on the volume of the emitting system. It is independent of the temperature of the system.

Information about the temperature of the system can be obtained by investigating the relative populations of states. As a function of the excitation energy E , the population of states can be written as

$$\frac{dn(E)}{dE} = Ne^{-E/T} \Delta\rho(E), \quad (14)$$

where N is a normalization constant and $\Delta\rho(E)$ denotes the density of states [Eq. (8)]. If the energy dependence of the phase shifts is dominated by a series of resonances, the density $\Delta\rho$ can be approximated as⁶¹

$$\Delta\rho(E) \propto \sum_i \frac{(2J_i + 1)\Gamma_i/2\pi}{(E - E_i)^2 + \Gamma_i^2/4}, \quad (15)$$

and the population of states decaying into the channel c can be written as

$$\left[\frac{dn(E)}{dE} \right]_c = Ne^{-E/T} \sum_i \frac{(2J_i + 1)\Gamma_i/2\pi}{(E - E_i)^2 + \Gamma_i^2/4} \frac{\Gamma_{c,i}}{\Gamma_i}, \quad (16)$$

where $\Gamma_{c,i}/\Gamma_i$ denotes the branching ratio for the decay into the channel c . In the limit of two nonoverlapping narrow states separated by an energy $\Delta E = E_2 - E_1$, the primary relative population of states, f_{12} , integrated over the widths of these states is given by

$$f_{12} = \frac{2J_2 + 1}{2J_1 + 1} e^{-\Delta E/T}. \quad (17)$$

In this approximation the relative population of states de-

pends only on the emission temperature of the system.

Historically, the sensitivity of two-particle correlation functions to the space-time extent of the emitting system was derived from the modifications of the wave functions of relative motion due to final-state interactions⁴⁰⁻⁴² or quantum statistics.³⁷⁻³⁹ If the time dependence of the emission process is neglected, one can express the two-particle correlation function in terms of the single particle source function $\rho(\mathbf{r})$ and the two-body wave function $\Psi(\mathbf{r}_1, \mathbf{r}_2)$:

$$R(q) = \int d^3r_1 d^3r_2 [|\Psi(\mathbf{r}_1, \mathbf{r}_2)|^2 - 1] \cdot \rho(\mathbf{r}_1) \rho(\mathbf{r}_2) \times \left[\int d^3r \rho(\mathbf{r}) \right]^{-2}. \quad (18)$$

This formula has recently been shown⁴² to be consistent with the thermal model, Eq. (11). For our calculations of the correlation functions, we have adopted the original formulation of Koonin, Eq. (18), and assumed a source of Gaussian spatial density, $\rho(r) \propto \exp(-r^2/r_0^2)$, and negligible lifetime.

B. Experimental correlation functions

In this subsection we present the two-particle correlation functions measured in this experiment. Apart from the energy thresholds no constraints were applied. The normalization constants, C_{12} [see Eq. (4)], extracted for the different particle combinations are rather similar; they do not vary by more than $\pm 15\%$ from their average value. This similarity indicates that different particle pairs have their origin in similar processes.

The two-proton correlation function, Fig. 3, exhibits a maximum at $q \approx 20$ MeV/c which is caused by the attractive singlet S -wave interaction between the two detected protons. Loosely speaking, one may also consider this maximum as due to the emission of particle unstable ${}^2\text{He}$ nuclei.^{33,62}

The p-t correlation function, Fig. 4, exhibits two maxima, corresponding to the decay of the $J^\pi = 0^+$ state⁶³ at 20.1 MeV ($\Gamma_p/\Gamma = 1.00$) and the two overlapping $J^\pi = 0^-$ and 2^- states^{63,64} at 21.1 and 22.1 MeV in ${}^4\text{He}$ ($\Gamma_p \approx \Gamma_n$),

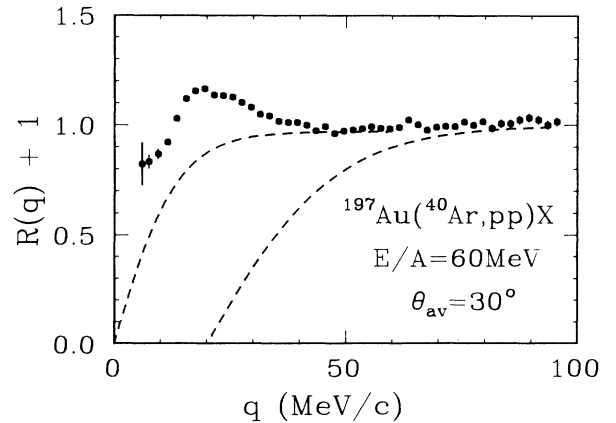


FIG. 3. Two-proton correlation function. The dashed lines are extreme bounds for the background correlation function.

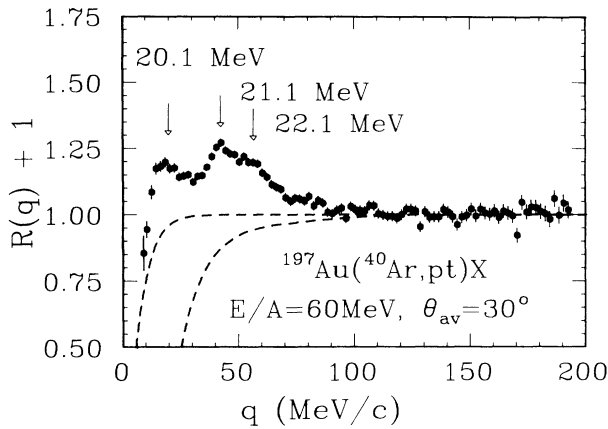


FIG. 4. p-t correlation function. Particle unstable states in ${}^4\text{He}$ are marked by the arrows. The dashed lines are extreme bounds for the background correlation function.

respectively. The d-t correlation function, Fig. 5, exhibits two maxima corresponding to highly excited levels in ${}^5\text{He}$ at 16.76 and 19.8 MeV excitation energy.⁶⁵ The slight shift of the peak corresponding to the 16.76 MeV state to higher relative momenta is an artifact of our data reduction in which it is assumed that the particles hit the center of each detector.

The p- ${}^3\text{He}$ correlation function, Fig. 6, exhibits a broad structure which corresponds to the “ground state” of ${}^4\text{Li}$.^{66,67} The increase at small relative momenta, $q \leq 15$ MeV/c, is probably due to the Coulomb final-state interaction between the residual nuclear system and the coincident protons and ${}^3\text{He}$ nuclei. For short lived states decaying into particles of different charge-to-mass ratios, this interaction can cause significant distortions of the line shape; also see Sec. IV D.

Figure 7 shows the measured p- α and d- ${}^3\text{He}$ correlation functions. The p- α correlation function, shown in Fig. 7(a), exhibits two pronounced peaks. The narrow struc-

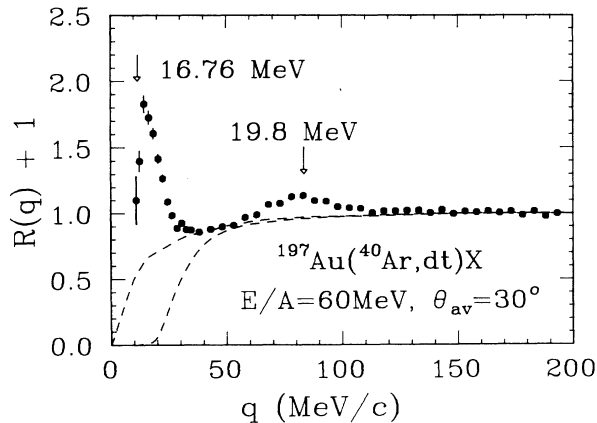


FIG. 5. d-t correlation function. Known levels in ${}^5\text{He}$ are indicated. The dashed lines are extreme bounds for the background correlation function.

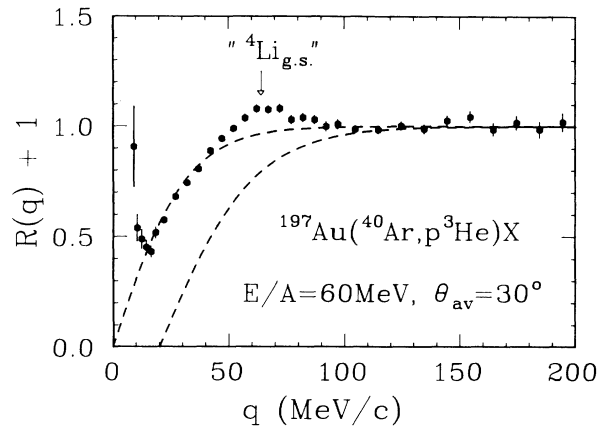


FIG. 6. p- ${}^3\text{He}$ correlation function. The location of the “ground state” of ${}^4\text{Li}$ is marked by the arrow. The dashed lines are extreme bounds for the background correlation function.

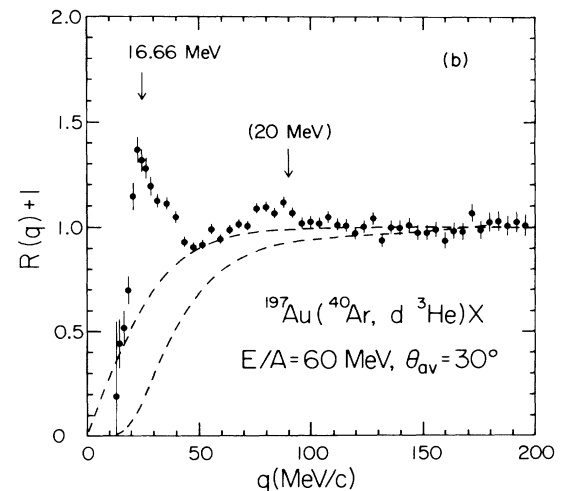
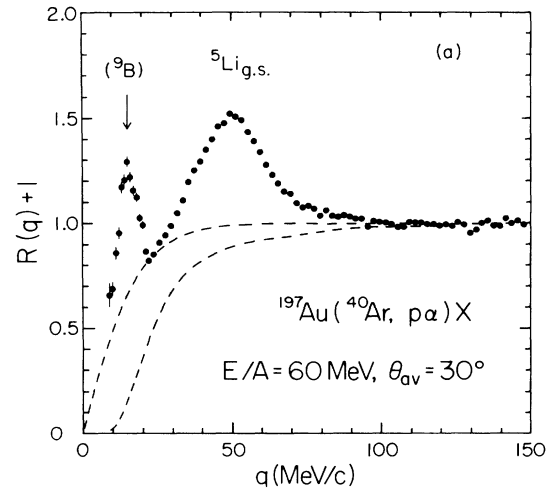


FIG. 7. (a) p- α and (b) d- ${}^3\text{He}$ correlation functions. Excited states in ${}^5\text{Li}$ are indicated. The dashed lines are extreme bounds for the background correlation function.

ture at $q \approx 15$ MeV/c is not related to a resonance in the mass five system. It results⁵² from the decay of the particle unstable ground state of ${}^9\text{B}$, ${}^9\text{B} \rightarrow 2\alpha + p$; also see Sec. IV D. The broad peak near $q \approx 50$ MeV/c is related to the unbound ground state of ${}^5\text{Li}$ ($J^\pi = \frac{3}{2}^-$, $\Gamma \approx 1.5$ MeV, $\Gamma_p/\Gamma = 1.00$). The largest peak in the d- ${}^3\text{He}$ correlation function, Fig. 7(b), corresponds to the decay of the 16.66 MeV state in ${}^5\text{Li}$ ($J^\pi = \frac{3}{2}^+$, $\Gamma \approx 0.3$ MeV, $\Gamma_d/\Gamma = 0.86$).

The d- α correlation function, Fig. 8, exhibits two maxima which correspond to the $T=0$ state in ${}^6\text{Li}$ at 2.186 MeV ($J^\pi = 3^+$, $\Gamma = 24$ keV, $\Gamma_\alpha/\Gamma_{\text{tot}} = 1.00$) and the overlapping $T=0$ states at 4.31 MeV ($J^\pi = 2^+$, $\Gamma = 1.3$ MeV, $\Gamma_\alpha/\Gamma_{\text{tot}} = 0.97$) and at 5.65 MeV ($J^\pi = 1^+$, $\Gamma = 1.9$ MeV, $\Gamma_\alpha/\Gamma_{\text{tot}} = 0.74$).

The t- α correlation function, Fig. 9, is dominated by the narrow $J^\pi = \frac{7}{2}^-$ state in ${}^7\text{Li}$ at 4.630 MeV ($\Gamma = 93$ keV, $\Gamma_\alpha/\Gamma_{\text{tot}} = 1.00$). In addition, the correlation function exhibits a broad structure corresponding to overlapping states in ${}^7\text{Li}$ at 6.68, 7.46, and 9.67 MeV.⁶⁵ Additional contributions may be due to a less well established state at 8.81 MeV and several other broad states at about 10 MeV excitation energy.^{68,69}

The ${}^3\text{He}$ - α correlation function, Fig. 10, shows a pronounced peak resulting from the decay of the 4.57 MeV state in ${}^7\text{Be}$ ($J^\pi = \frac{7}{2}^-$). The broad maximum at $q \approx 125$ MeV/c corresponds to broad states⁶⁵ in ${}^7\text{Be}$ at 6.73 and 7.21 MeV. The rise at $q < 40$ MeV/c is probably due to a 2% contamination of the coincident ${}^3\text{He}$ spectrum by α particles resulting from the decay of the ${}^8\text{Be}$ ground state; this region will be excluded from the analysis.

Figure 11 shows the α - α [panel (a)] and p- ${}^7\text{Li}$ [panel (b)] correlation functions. The α - α correlation function is dominated by the decay of the particle unstable ground state⁶⁵ of ${}^8\text{Be}$ ($J^\pi = 0^+$, $\Gamma = 6.8$ eV, $\Gamma_\alpha/\Gamma = 1.00$). The peak at $q \approx 105$ MeV/c corresponds to the decay of the 3.04 MeV state⁶⁵ in ${}^8\text{Be}$ ($J^\pi = 2^+$, $\Gamma = 1.5$ MeV, $\Gamma_\alpha/\Gamma = 1.00$). The pronounced structure at $q \approx 50$ MeV/c is not directly associated with a state in ${}^8\text{Be}$. It is largely

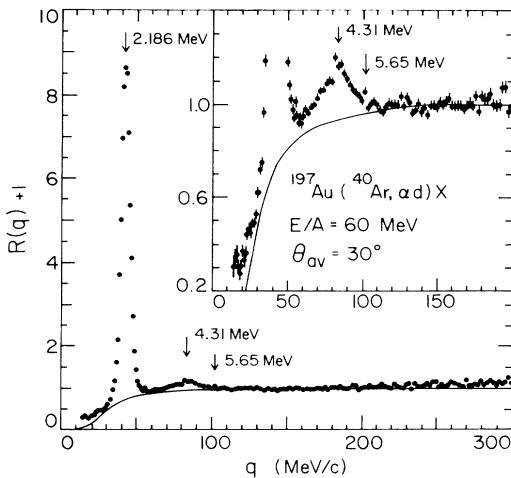


FIG. 8. d- α correlation function. Excited states in ${}^6\text{Li}$ are indicated. The curve represents the background correlation function.

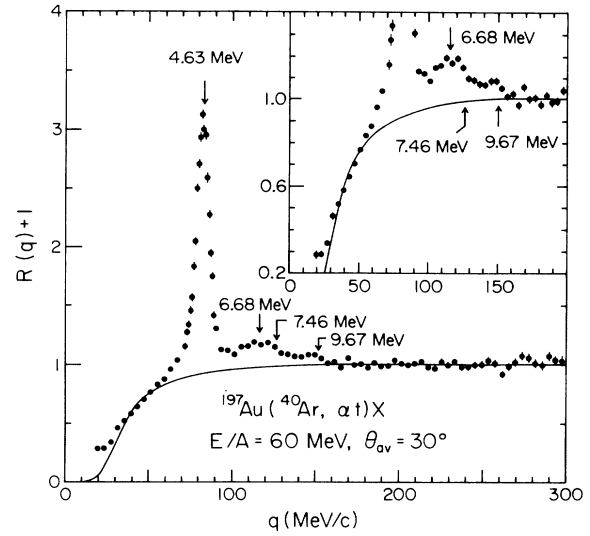


FIG. 9. t- α correlation function. Excited states in ${}^7\text{Li}$ are indicated. The curve represents the background correlation function.

due to the decay⁷⁰ of the 2.43 MeV state⁶⁵ in ${}^9\text{Be}$; in addition, it contains contributions from the “ghost peak”^{71–73} of the ${}^8\text{Be}$ ground state; see Sec. IV E. The p- ${}^7\text{Li}$ correlation function exhibits several sharp structures resulting from the decay of high lying states in ${}^8\text{Be}$ at excitation energies of 17.64 MeV and higher. For our analysis, we will use the first two peaks⁶⁵ at 17.64 MeV ($J^\pi = 1^+$, $\Gamma = 0.01$ MeV, $\Gamma_p/\Gamma_{\text{tot}} = 1.00$) and at 18.15 MeV ($J^\pi = 1^+$, $\Gamma = 0.14$ MeV, $\Gamma_{p_0}/\Gamma_{\text{tot}} = 0.96$).

An example for the population of particle unbound states in ${}^{11}\text{B}$ decaying into the α - ${}^7\text{Li}$ channel is shown in Fig. 12. Although we cannot resolve the individual levels in ${}^{11}\text{B}$, the regions of $35 \leq q \leq 68$ MeV/c and $68 < q \leq 100$ MeV/c are clearly dominated by the states⁶⁵ at 9.185 and 9.2744 MeV and 9.876, 10.26, 10.33, and 10.597 MeV, respectively.

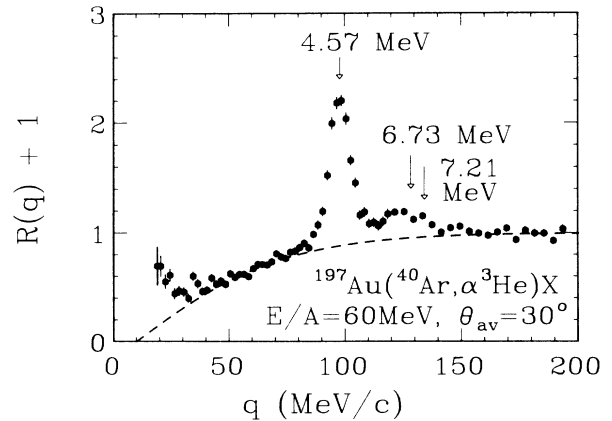


FIG. 10. ${}^3\text{He}$ - α correlation function. States in ${}^7\text{Be}$ are indicated. The dashed curve represents the background correlation function.

Examples for two-particle correlations which are not dominated by resonant interactions are shown in Fig. 13. These correlations are dominated by the long-range Coulomb repulsion. The rise of the p-d correlation function at small relative momenta, $q \leq 15$ MeV/c, is caused by the final-state interaction of the coincident protons and deuterons with the Coulomb field of the heavy reaction residue;⁷⁴ see Sec. IV D.

C. Source radii

In this subsection we extract source dimensions from the measured two-particle correlation functions using the final-state interaction model,^{40,45,47} Eq. (18). Since different particle pairs and particles of different energies may be emitted at different stages of the reaction,^{43,47,48} one may hope to extract detailed information about the

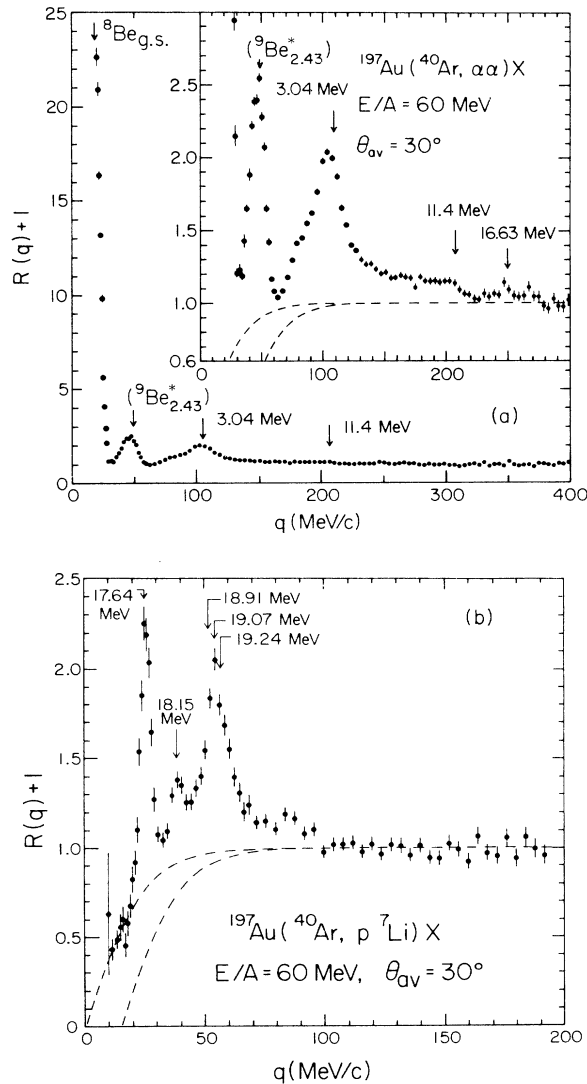


FIG. 11. (a) α - α and (b) p- ^7Li correlation functions. Excited states in ^8Be are indicated. The dashed lines are extreme bounds for the background correlation function.

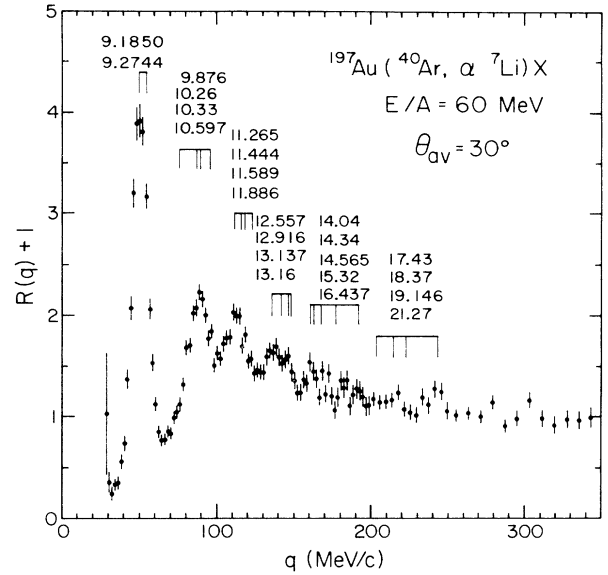


FIG. 12. α - ^7Li correlation function. Excited states in ^{11}B which decay into the α - ^7Li channel are indicated.

reaction by exploring the energy dependence of correlation functions measured for different particle pairs.

Figures 14–16 show examples of two-particle correlation functions for different constraints on the total kinetic energy, $E_1 + E_2$, of the coincident particles. The constraints are indicated in the figures. The normalization constants, C_{12} , in Eq. (4) were taken as independent of these constraints. Whenever the interaction between the two particles is dominated by a resonance, the maxima of the corresponding correlation functions increase with increasing total kinetic energy; see the examples given in Figs. 14 and 16. For repulsive interactions, $\partial\delta/\partial q < 0$, the correlation functions exhibit more pronounced minima for increasing total kinetic energies; see the example given in Fig. 15. This general energy dependence of the two-particle correlation functions may indicate that more energetic light particles are emitted from sources which are

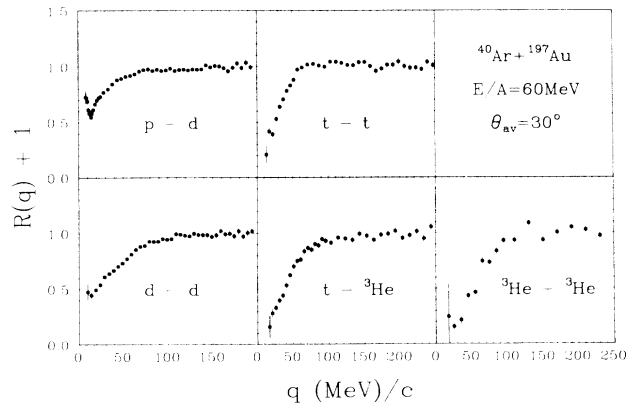


FIG. 13. p-d, d-d, t-t, t - ^3He , and ^3He - ^3He correlation functions.

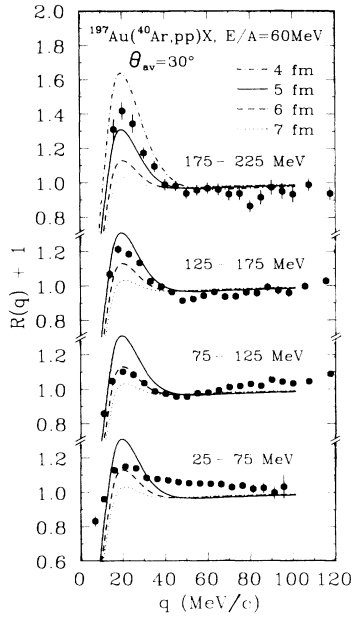


FIG. 14. Two-proton correlation functions for different constraints on the sum energy, $E_1 + E_2$. The curves show calculations with the final state interaction model, Eq. (18).

more localized in space time.

The curves in Figs. 14–16 correspond to theoretical correlation functions predicted by the final-state interaction model,^{40,45,47} Eq. (18). The theoretical d- α correlations, Fig. 16, were corrected for the finite resolution of the hodoscope by folding the calculations with the resolu-

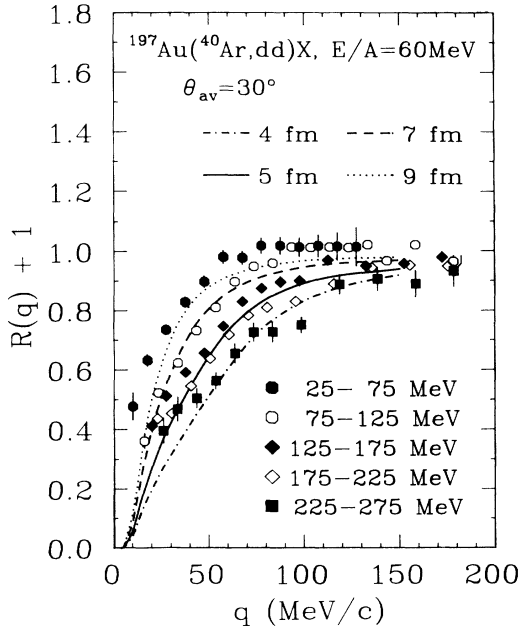


FIG. 15. Two-deuteron correlation functions for different constraints on the total kinetic energy, $E_1 + E_2$. The curves show calculations with the final state interaction model, Eq. (18).

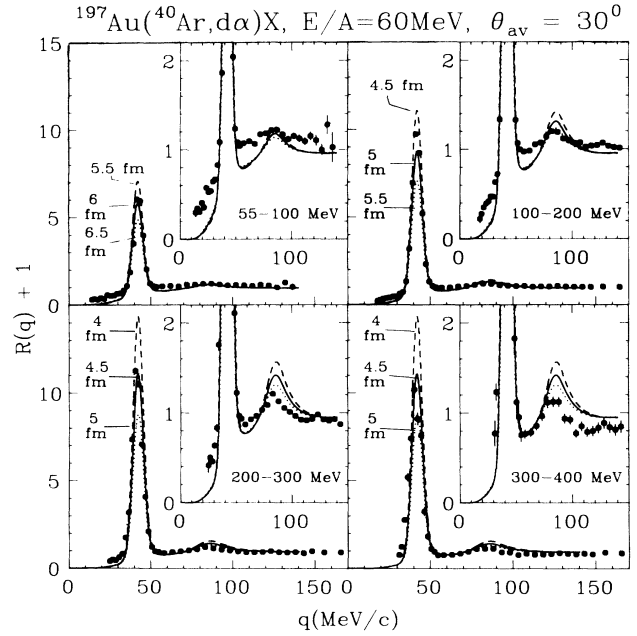


FIG. 16. d- α correlation functions for different constraints on the sum energy, $E_1 + E_2$. The curves show calculations with the final state interaction model, Eq. (18).

tion function of the hodoscope. The estimated source radii r_0 are summarized in Table II. Also included in the table are the results from similar analyses of the t-t and p- α correlation functions. The errors include normalization uncertainties for the different energy gates which were evaluated by normalizing the experimental correlation functions to the calculations at large relative momenta. Generally, the extracted radii are larger than the size⁷⁵ of the target nucleus,

$$r_0(\text{Au}) = \sqrt{2/3} r_{\text{rms}}(\text{Au}) \approx 4.4 \text{ fm} .$$

The source dimensions approach the size of target nucleus only for the highest total kinetic energies. The smallest source radii are extracted from d- α and p-p correlations. Significantly larger source dimensions are extracted from two-deuteron correlations, possibly indicating smaller freeze-out densities for particles with larger interaction cross sections.^{46,47}

Our findings may indicate the sequential freeze-out of different particle species at different stages of the reaction.^{47,48} However, several uncertainties remain for the interpretation of two-particle correlations: (i) Sequential feeding from highly excited primary fragments may alter the two-particle correlation function. Because of the finite lifetime of possible long-lived intermediate reaction products, sequential decays could lead to a damping of the experimental correlation functions and simulate large source dimensions. Sequential feeding could, however, also increase structures in the correlation functions if the decays proceed via the corresponding resonance. (ii) Collisions with different impact parameters may correspond to sources with different space-time dimensions and/or different relative particle abundances.¹⁴ Different energy

TABLE II. Source radii, r_0 , for a source of negligible lifetime and Gaussian density distribution, $\rho(r)=\rho_0\exp(-r^2/r_0^2)$, extracted from two-particle correlation functions by using the final-state interaction model, Eq. (18). The errors include normalization uncertainties for the different energy gates.

| Pair | E_1+E_2 (MeV) | r_0 (fm) |
|--------------------|--------------------|---------------------|
| p + p | 25–75 | $6_{-1.0}^{+0.5}$ |
| | 75–125 | 6 ± 0.5 |
| | 125–175 | 5.5 ± 0.4 |
| | 175–225 | 4.6 ± 0.3 |
| d + d | 25–75 | 10 ± 3 |
| | 75–125 | 7 ± 2 |
| | 125–175 | 6 ± 2 |
| | 175–225 | 5 ± 1 |
| t + t ^a | 225–275 | 4 ± 1 |
| | 36–100 | 7.5 ± 1.5 |
| | 100–180 | 6 ± 1.5 |
| | 180–260 | 6 ± 1.5 |
| p + α | 52–125 | $7.5_{-1.0}^{+0.5}$ |
| | 125–200 | 6.7 ± 0.4 |
| | 200–300 | 5.9 ± 0.3 |
| d + α | 300–400 | 4.4 ± 0.2 |
| | 55–100 | 5.7 ± 0.2 |
| | 100–200 | 4.8 ± 0.2 |
| | 200–300 | 4.3 ± 0.2 |

^aThe calculations include a nuclear potential only for the $l=0$ partial wave; see Ref. 45 for more details.

regions may be biased towards certain reaction mechanisms.⁷⁶ (iii) The calculations of theoretical two-particle correlation functions may have non-negligible uncertainties due to uncertainties of the low energy phase shifts.^{45,46} (iv) The present calculations are still rather schematic. Consistent treatments of the temporal and dynamical evolution of the emitting source would clearly be desirable. Since finite lifetime effects will lead to reduced correlations, the extracted source radii may only establish upper limits for the spatial extent of the emitting system. On the other hand, an explosive expansion of the source could enhance the correlations for more energetic particles.⁵⁰ Moreover, the effects of the (long-range) Coulomb interaction with the residual nuclear matter have been neglected.

D. Three-body Coulomb interactions

Two particles with different charge-to-mass ratios experience different accelerations in the Coulomb field of the residual nuclear system. For short-lived decays, two-particle correlations at small relative momenta can, therefore, be distorted by the interaction of the coincident particles with this external field.^{51,52}

Figure 17 illustrates the Coulomb distortions of the p- α correlation function.⁵² The open and solid points show the correlation functions measured for the constraints $v_\alpha < v_p$ and $v_\alpha > v_p$, respectively, where v_α and v_p denote the laboratory velocities of alpha particles and protons.

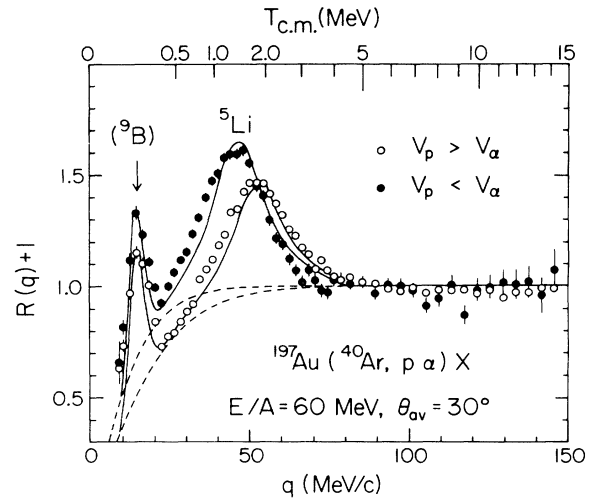


FIG. 17. p- α correlation functions gated by constraints on v_α and v_p , the laboratory velocities of the alpha particles and protons.

While the location of the maximum of the correlation function at $q \approx 15$ MeV/c remains constant, the location of the maximum at $q \approx 50$ MeV/c is shifted for the two kinematic branches. The peak near $q \approx 15$ MeV/c is due⁵² to the two-stage decay of ${}^9\text{B}$: ${}^9\text{B}_{\text{g.s.}} \rightarrow \text{p} + {}^8\text{Be}_{\text{g.s.}} \rightarrow \text{p} + (\alpha + \alpha)$; it results from the small decay energies and the narrow widths of the ground states of ${}^9\text{B}$ and ${}^8\text{Be}$. Because of the long lifetime of ${}^9\text{B}_{\text{g.s.}}$, the Coulomb interaction of its decay products with the heavy reaction residue is negligible. The broad peak near $q \approx 50$ MeV/c is due to the unbound ground state of ${}^5\text{Li}$. Because of the short mean lifetime of ${}^5\text{Li}_{\text{g.s.}}$ ($\tau=130$ fm/c), its decay takes place in the Coulomb field of the heavy reaction residue. Due to their greater charge-to-mass ratio, protons will experience a greater acceleration in this Coulomb field than alpha particles. Qualitatively, the velocity difference between protons and alpha particles will be decreased if $v_p < v_\alpha$ at the time of decay, while the difference will be increased if $v_p > v_\alpha$. The curves shown in the figure correspond to calculations which take these final-state Coulomb interactions into account.⁵² It was assumed that the coincidence cross section consists of three terms: $\sigma_{\text{ap}} = \sigma_{9\text{B}} + \sigma_{5\text{Li}} + \sigma_b$, where $\sigma_{9\text{B}}$ and $\sigma_{5\text{Li}}$ denote the contributions from the decay of ${}^9\text{B}$ and ${}^5\text{Li}$ nuclei and σ_b denotes the “background” cross section; details of the calculations were given in Ref. 52. The choices of background are shown by the dashed curves in Fig. 17. A consistent description of the α -p correlation function could only be obtained by assuming slightly different background correlation functions for the two kinematic branches. These differences, too, could be due to Coulomb interactions with the field of the heavy reaction residue.

For the case of nonresonant final-state interactions between the two coincident particles, no long-lived intermediate states are formed. Therefore, the two-particle correlation function should be sensitive to the relative locations of the emitted particles with respect to the heavy

reaction residue.⁷⁴ An example of such an effect can be given for the p-d correlation function. Figure 18(a) shows a contour diagram of the two-dimensional proton-deuteron correlation function, $R(E_p, E_d)$, defined in analogy to Eq. (4):

$$\sum Y_{pd}(E_p, E_d) = C[1 + R(E_p, E_d)] \sum Y_p(E_p) Y_d(E_d). \quad (19)$$

The indices p and d denote protons and deuterons, respectively; E is the energy of the detected particles. The summation in Eq. (19) is performed over all angles and energies corresponding to $\Delta\theta = 4.2^\circ$ and the given bins of E_p and E_d . $R(E_p, E_d)$ exhibits a clear minimum for small relative velocities, $v_p \approx v_d$, which is caused by the repulsive proton-deuteron Coulomb interaction. The exact location of the minimum is, however, displaced from the line of minimum relative velocity, $v_p \approx v_d$, for small relative angles ($\Delta\theta = 4.2^\circ$); see dashed line in Fig. 18(a). Following Ref. 74, we introduce new coordinates S and T measured along axes perpendicular and parallel to the line $v_p = v_d$:

$$\begin{aligned} S &= (\alpha E_p - E_d) / (1 + \alpha^2)^{1/2}, \\ T &= (E_p + \alpha E_d) / (1 + \alpha^2)^{1/2}, \end{aligned} \quad (20)$$

where $\alpha = m_d/m_p$. In terms of these coordinates, the line $E_d = \alpha E_p$ corresponds to $S = 0$. The displacement of the minimum of the correlation function from the line $S = 0$ is related to the Coulomb potential at the point of emission.

For a quantitative determination of this displacement, we use correlation functions defined in terms of the coordinates S and T :

$$\sum Y_{pd}(S, T) = C[1 + R(S)] \sum Y_p[E_p(S, T)] Y_d[E_p(S, T)]. \quad (21)$$

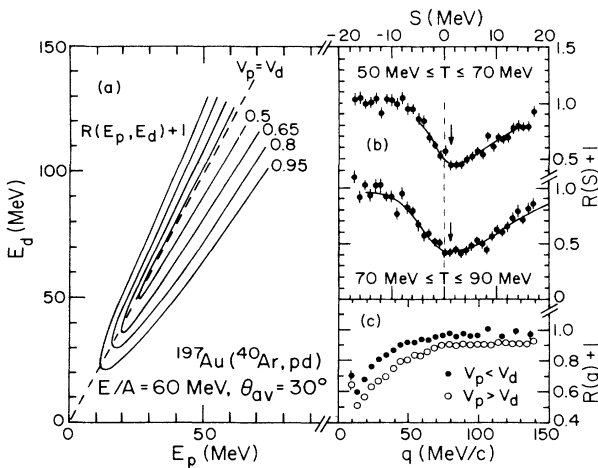


FIG. 18. p-d correlation functions for $\Delta\theta = 4.2^\circ$. (a) Two-dimensional correlation matrix. (b) Correlation functions as a function of the coordinate S [Eq. (20)]. (c) Correlation functions as a function of the momentum of relative motion, q , with constraints on v_p and v_d .

As before, the summation is performed over all detector pairs with $\Delta\theta = 4.2^\circ$. The resulting correlation functions $R(S)$ are shown in Fig. 18(b). Gates on T , indicated in the figure, were applied to the summation in Eq. (21). The location, S_c , of the minimum of $R(S)$ exhibits no significant dependence on T .

Three-body Coulomb trajectory calculations similar to those described in Ref. 74 indicate that the average experimental shift, $\langle S_c \rangle \approx 1.0_{-0.5}^{+1.0}$, can be accounted for if the particles are assumed to be emitted at distances, $d < 50$ fm, from the heavy reaction residue; within the experimental uncertainty one cannot exclude emission from a point close to the surface of the composite system. Such small distances exclude significant contributions to the p-d coincidence yield from the decay of long-lived projectile fragments; however, emission from broad states ($\Gamma \geq 2$ MeV) cannot be ruled out.

To complete the discussion of proton-deuteron correlations, we show in Fig. 18(c) the correlation function $R(q)$, Eq. (4), gated on the two kinematic regions $v_p > v_d$ (open points) and $v_p < v_d$ (solid points). These correlation functions support our argument concerning Coulomb distortions of the p- α background correlation function, Fig. 17. At small relative momenta, the correlation functions suffer particularly pronounced Coulomb distortions due to the displacement of the minimum of the correlation function, Fig. 18(a), from the line of minimum relative velocity. This displacement produces a rise of the correlation function, $R(q)$, at small relative momenta; see also Figs. 6 and 13. The distortions are sufficiently large to preclude the extraction of source radii from the p-d correlation function.

E. Ternary decays

Two particle correlation functions may exhibit spurious structures due to ternary decays. An example of a narrow structure which was caused by the two-stage decay of ^9B was discussed in connection with the α -p correlation function; see Fig. 17. As a less trivial example, we discuss the 2α correlation function, shown in Fig. 11(a). This correlation function exhibits a pronounced structure at $q \approx 50$ MeV/c which is not directly related to a state in ^8Be .

For a quantitative analysis, we assume that the total coincidence yield, $Y_{\alpha\alpha}$, can be expressed as $Y_{\alpha\alpha} = Y_c + Y_b$, where Y_c denotes the coincidence yield resulting from the decay of particle unbound states. The "background" yield, Y_b , was described in terms of a background correlation function, $R_b(q)$:

$$Y_b(q) = C_{12}[1 + R_b(q)] Y_1(\mathbf{p}_1) \cdot Y_2(\mathbf{p}_2). \quad (22)$$

The extracted decay coincidence yield, Y_c , is shown in the lower part of Fig. 19 as a function of relative kinetic energy, $T_{c.m.} = q^2/2\mu$. The background was assumed to lie within the boundaries corresponding to the dashed lines in Fig. 11(a). The size of the error bars indicates the uncertainty associated with the background function. The two peaks in the spectrum correspond to the ^8Be ground state and the structure at 50 MeV/c in Fig. 14(a). The lightly shaded area bounded by the dashed histogram represents the theoretical yield, $Y_c(^8\text{Be})$, resulting from the decay of

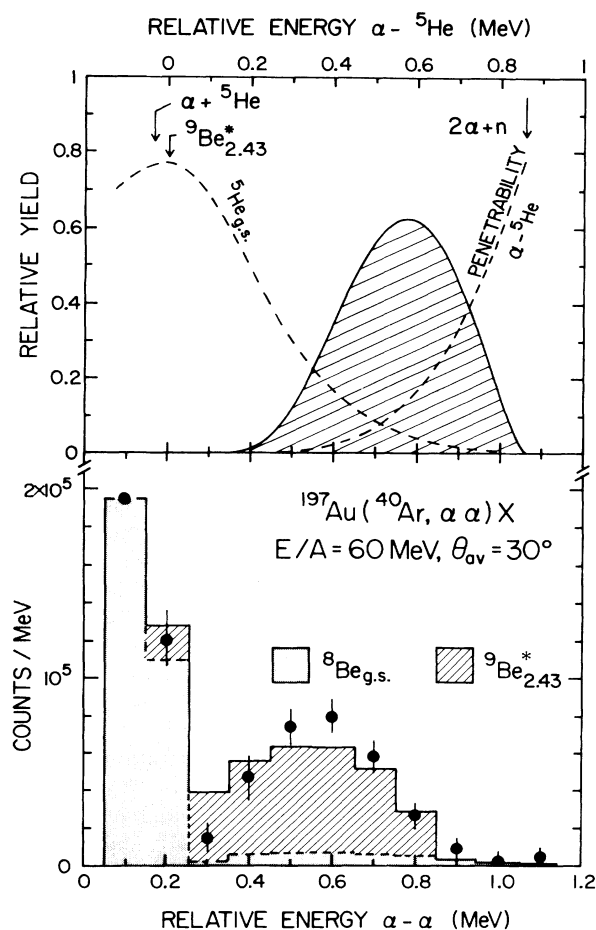


FIG. 19. Two-alpha-particle coincidence yield resulting from the decay of particle unstable states (lower panel); the dashed lines (shaded area) show the calculated yield from the decay of ${}^8\text{Be}_{g.s.}$; the solid lines (hatched area) show the calculated α - α yield resulting from the decay of ${}^9\text{Be}_{2.43}^*$. Details of this decay are illustrated in the top section of the figure.

${}^8\text{Be}$. Level parameters from Ref. 73 were used to describe the line shape of the ${}^8\text{Be}$ ground state and other higher lying states. The calculations took the exact detector efficiency into account; they were normalized to the data at the relative energy of 0.1 MeV. The calculations predict a weak structure at a relative energy $T_{c.m.} \approx 0.5$ MeV which is due to the “ghost peak” of the ${}^8\text{Be}$ ground state. (The ghost peak is caused^{71,72} by the small width of the ${}^8\text{Be}$ ground state, $\Gamma = 6.8$ eV, and the proximity of the α - α threshold.) The decay of ${}^8\text{Be}$ cannot explain the peak at $T_{c.m.} \approx 0.6$ MeV. The most likely origin of this peak is the decay of the 2.43 MeV state of ${}^9\text{Be}$: ${}^9\text{Be}_{2.43} \rightarrow {}^5\text{He} + \alpha \rightarrow 2\alpha + n$. The ${}^9\text{Be}$ decay probability can be approximated as⁷⁰

$$\frac{dn}{dT_{c.m.}^1}(T_{c.m.}^1) \propto P_2(T_{c.m.}^1) \rho_{5\text{He}}^*(E_{5\text{He}}^*), \quad (23)$$

where $T_{c.m.}^1$ is the relative kinetic energy ($T_{c.m.}^1 \leq 0.855$ MeV), P_2 is the $l=2$ Coulomb penetration factor evaluat-

ed for a radius of 4.5 fm, and $\rho_{5\text{He}}$ is the intrinsic distribution of the ${}^5\text{He}_{g.s.}$ calculated at the energy $E_{5\text{He}}^* = 0.886$ MeV - $T_{c.m.}^1$ above the α - n threshold. The line shape of ${}^5\text{He}$ was described in terms of the level parameters given in Ref. 77. Both the ${}^5\text{He}$ line shape and the α - ${}^5\text{He}$ penetration factor are shown in the upper part of Fig. 19; the product, $dn/dT_{c.m.}^1$, is indicated by the dashed area: The strong variation of the penetrability in the tail region of the ${}^5\text{He}$ ground state produces a relatively narrow window for this decay.

Assuming isotropic decay for both steps of the decay, ${}^9\text{Be}_{2.43} \rightarrow {}^5\text{He} + \alpha \rightarrow 2\alpha + n$, and including the detector efficiency of our hodoscope for the detection of the two alpha particles we obtained the 2α yield indicated by the dashed area in the lower part of Fig. 19. The yield was normalized to the missing yield, $Y_c - Y_{8\text{Be}}$, integrated over the range $0.3 \leq T_{c.m.} \leq 1.1$ MeV. Not included in our calculations is the final-state Coulomb interaction between the two alpha particles⁷⁸ which will, on average, increase their relative energy. Considering the neglect of this effect, the calculation describes the position and shape of the structure at $T_{c.m.} \approx 0.6$ MeV rather well.

V. POPULATIONS OF PARTICLE UNSTABLE STATES

A. Response of the hodoscope

Information about the excitation energy density or “emission temperature” of highly excited nuclear systems can be extracted from the relative populations of excited states, see Eqs. (14)–(16). In this section we will describe and justify the procedure which we have adopted to quantitatively determine the production of nuclei in particle unstable states.

The coincidence yield, Y_c , resulting from the decay of particle unstable states is assumed to be given by $Y_c = Y_{12} - C_{12} Y_1 Y_2 [1 + R_b(q)]$, where $R_b(q)$ denotes the background correlation function, Eq. (22). Since there is no unique description for calculating the background correlation function, we have chosen empirical background correlation functions. To estimate the errors due to uncertainties of the background, we varied $R_b(q)$ within reasonable limits and calculated the effects on the final results. The extremes within which the background functions were assumed to lie are indicated in Figs. 4–11. (When the choice of the background is not very crucial, only the “most likely” shape is shown.)

As an example, Fig. 20 shows the coincidence yields extracted for the decay of particle unstable ${}^6\text{Li}$ nuclei as a function of the relative kinetic energy, $T_{c.m.}$, in the ${}^6\text{Li}$ rest frame; only statistical errors are shown. For orientation, the excitation energy in ${}^6\text{Li}$ is given by the upper scale.

The experimental yield Y_c is related to the excitation energy spectrum decaying into the channel c , $[dn(E)/dE]_c$, by the relation

$$Y_c(E') = \int dE \left[\epsilon_c(E', E) \left(\frac{dn(E)}{dE} \right)_c \right]. \quad (24)$$

Here, $\epsilon_c(E', E)$, is the efficiency function of the hodo-

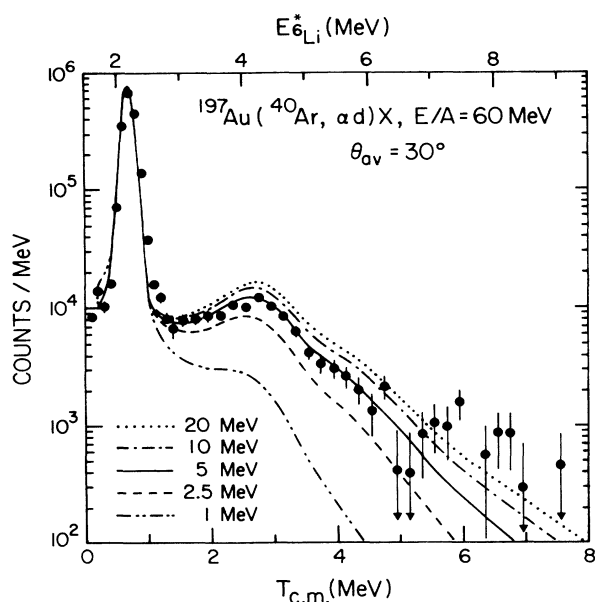


FIG. 20. Energy spectrum resulting from the decay of particle-unstable states in ${}^6\text{Li}$. The curves correspond to thermal distributions, Eq. (25), with $T=1, 2.5, 5, 10,$ and 20 MeV.

scope; E and E' are the actual and measured excitation energies, respectively. (The excitation energy E and the relative kinetic energy, $T_{c.m.}$, are related to the separation energy, Q_s , via $E = T_{c.m.} + Q_s$.) The efficiency functions for our hodoscope were determined by detailed Monte Carlo calculations. These calculations take into account the precise geometry of the hodoscope, the angular straggling in the target, the measured detector energy resolutions, and the constraints on the particle energies. The decays of the parent nuclei were assumed to be isotropic in their center-of-mass frames. The laboratory energy spectra and angular distributions of the parent nuclei were described by simple moving-source parametrizations, Eq. (3). When stable parent nuclei exist (e.g., α particles and ${}^6\text{Li}$ nuclei) these parametrizations were constrained to reproduce the experimental distributions. In order to obtain an optimum analytical description of the spectral shape, only the angular range covered by the hodoscope

($\theta \approx 22.7^\circ - 37.3^\circ$) was included in the fits. The resulting parameters for the three “moving sources” are listed in Table III. (Because of the limited angular range, the parameters of these fits are not equivalent to the parameters given in Table I.) For parent nuclei with particle unstable ground states (e.g., ${}^3\text{He}$, ${}^5\text{Li}$, and ${}^8\text{Be}$) source parameters of neighboring stable nuclei (α , ${}^6\text{He}$, ${}^6\text{Li}$, and ${}^7\text{Li}$) were used. This procedure may be justified by the similarity of the source parameters for different fragments;¹⁸ see also Table I. Since emission temperatures are determined from the *relative* populations of states, only *relative* efficiencies need to be known. The extracted emission temperatures are, therefore, not very sensitive to details of the parent distributions.

For illustration, Fig. 21 shows calculations for the integral efficiency, $\hat{\epsilon}(E) = \int dE' \epsilon(E', E)$, and the rms resolution, $\delta T_{c.m.}$, for the decay of ${}^6\text{Li} \rightarrow \alpha + d$. The efficiency (upper part) is normalized to 1 at the relative kinetic energy, $T_{c.m.} = 0.711$ MeV, which corresponds to the first excited state in ${}^6\text{Li}$. Monte Carlo calculations of the resolution function, which disregard angular straggling of the decay products in the target, are shown by the dashed line. The resolution of the present hodoscope is mainly limited by the finite opening angles of the individual telescopes; angular straggling in the target is less important. The calculations are in good agreement with the experimental width for the 2.186 MeV state in ${}^6\text{Li}$, $\delta T_{c.m.} \approx 95$ keV. For this narrow state ($\Gamma = 24$ keV) the observed width is determined by the instrumental resolution.

Integrated efficiencies and population ratios are not sensitive to angular straggling in the target. Therefore, most of our efficiency functions were determined without CPU-time intensive angular straggling calculations. It was verified that this omission does not affect the final results.

To test the assumptions of our Monte Carlo calculations, we examined the decay ${}^6\text{Li}_{2.186}^* \rightarrow \alpha + d$. Figure 22 shows the total kinetic energy distribution, $dY_c/d(E_\alpha + E_d)$, integrated over the first peak in the ${}^6\text{Li}$ excitation energy spectrum, $T_{c.m.} = 0.3 - 1.2$ MeV. The yields predicted by the Monte Carlo calculations are shown by the solid histogram. Within the uncertainties of the primary energy distributions²⁷ of stable ${}^6\text{Li}$ nuclei at energies below ≈ 80 MeV and above ≈ 350 MeV, the data are consistent with our assumptions of the parent energy distribution.

TABLE III. Parameters for the three-source fits, Eq. (3), of the single particle inclusive spectra over the angular range covered by the hodoscope. N_1, N_2, N_3 in arbitrary units.

| Particle | U_C (MeV) | T_1 (MeV) | v_1 (c) | N_1 | T_2 (MeV) | v_2 (c) | N_2 | T_3 (MeV) | v_3 (c) | N_3 |
|-----------------|----------------|----------------|--------------|-------|----------------|--------------|-------|----------------|--------------|-------|
| p | 5 | 5.0 | 0.013 | 6422 | 11.4 | 0.261 | 1394 | 11.4 | 0.265 | 803 |
| d | 5 | 5.3 | 0.023 | 768 | 20.4 | 0.115 | 557 | 10.0 | 0.273 | 1252 |
| t | 5 | 9.5 | 0.001 | 1179 | 17.5 | 0.163 | 524 | 8.2 | 0.289 | 1159 |
| ${}^3\text{He}$ | 10 | 8.9 | 0.002 | 563 | 16.5 | 0.219 | 307 | 6.7 | 0.328 | 910 |
| α | 10 | 9.2 | 0.064 | 1057 | 17.2 | 0.132 | 1979 | 11.2 | 0.266 | 757 |
| ${}^6\text{He}$ | 10 | 15.5 | 0.071 | 87 | 16.9 | 0.181 | 32 | 14.1 | 0.264 | 27 |
| ${}^6\text{Li}$ | 15 | 23.2 | 0.065 | 71 | 23.0 | 0.108 | 16 | 18.3 | 0.228 | 53 |
| ${}^7\text{Li}$ | 15 | 20.4 | 0.109 | 148 | 17.7 | 0.204 | 63 | 11.3 | 0.275 | 206 |

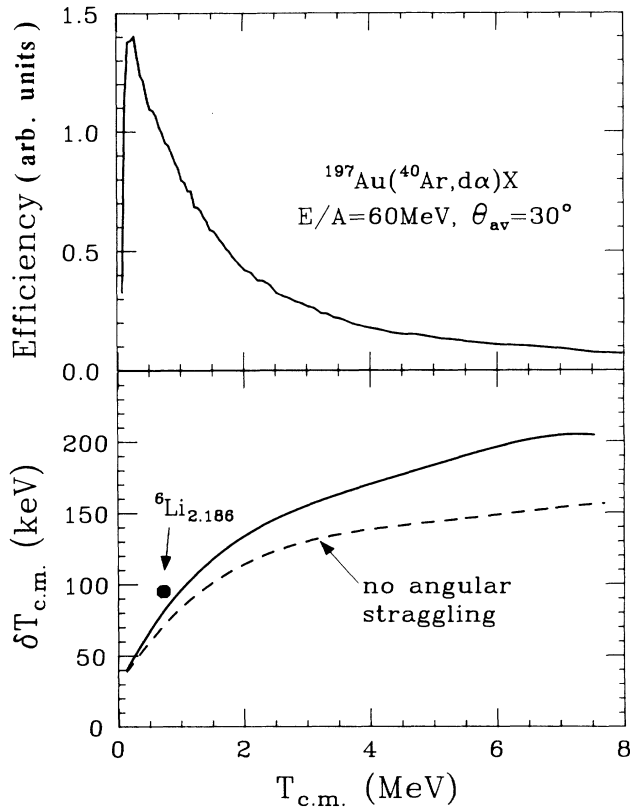


FIG. 21. Calculated integral efficiency (upper part) and rms resolution (lower part) for the detection of $d\text{-}\alpha$ pairs resulting from the decay of particle unstable ${}^6\text{Li}$. The efficiency has been normalized to 1 for the decay of ${}^6\text{Li}_{2.186}^*$. The point shows the experimental width for this decay.

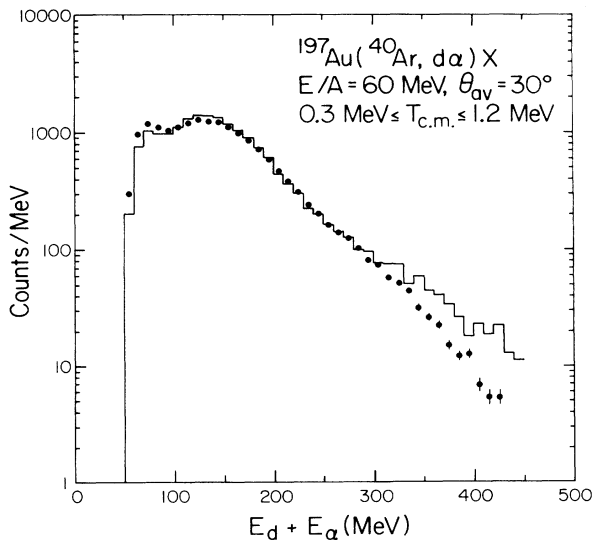


FIG. 22. Observed coincidence yield resulting from the decay ${}^6\text{Li}_{2.186}^* \rightarrow d + \alpha$ as a function of the total kinetic energy $E_\alpha + E_d$. The histogram is the result of the Monte Carlo calculations described in the text.

Angular distributions, $dY_c/d\theta_R$ and $dY_c/d\phi_R$, of the decay yields from the 2.186 MeV state in ${}^6\text{Li}$ are shown in Fig. 23. Here, θ_R is defined by

$$\cos(\theta_R) = (\mathbf{P} \cdot \mathbf{q}) / (|\mathbf{P}| \cdot |\mathbf{q}|),$$

where $\mathbf{P} = \mathbf{p}_1 + \mathbf{p}_2$ is the total momentum; ϕ_R is defined by

$$\cos(\phi_R) = [(\mathbf{n}_b \times \mathbf{P}) \cdot \mathbf{q}] / (|\mathbf{n}_b \times \mathbf{P}| \cdot |\mathbf{q}|),$$

where \mathbf{n}_b is a unit vector parallel to the beam direction. The histograms show the results of our Monte Carlo calculations. (The asymmetry of $dY_c/d\phi_R$ with respect to $\phi_R = 90^\circ$ is caused by the binning during the analysis of the experimental and as well as the simulated data.) Details of the θ_R distribution are sensitive to uncertainties in the absolute energy calibration. Within these uncertainties, the data are consistent with the assumption of isotropic decay.

We also investigated angular distributions for the decays ${}^5\text{Li}_{g.s.} \rightarrow \alpha + p$, ${}^9\text{Be}_{g.s.} \rightarrow 2\alpha + p$, and ${}^8\text{Be}_{g.s.} \rightarrow 2\alpha$. Each of these was consistent with the assumption of isotropic decay. No evidence could be established for significant spin alignments.

B. Mean emission temperatures

Within the thermal model, the relative populations of particle unstable states can be used to determine the temperature at the point at which the particles leave the equilibrated system. The equilibrium distribution of particle unbound states is given by Eqs. (14)–(16). Using Eq. (24), the coincidence yield due to the decay of thermally populated particle unstable states is obtained as

$$Y_c(E') = \int dE \epsilon_c(E', E) \times \left\{ \frac{N}{\pi} e^{-E/T} \sum_i \left[\frac{(2J_i + 1)(\Gamma_i/2)}{(E - E_i)^2 + \Gamma_i^2/4} \frac{\Gamma_{c,i}}{\Gamma_i} \right] \right\}. \quad (25)$$

In principle, the formal width of the level, $\Gamma_i = 2P_{li}\gamma_i^2$, and the resonance energy, $E_i = E_R + \Delta_{li}$, are functions⁷⁹ of the excitation energy E . Their energy dependence is expressed in terms of the penetrability P_{li} and shift function Δ_{li} . We will extract the populations of particle unstable states by integrating the experimental yield over the range of energies dominated by the corresponding resonances. Therefore, our results do not depend on a detailed description of the spectral shape. Unless stated otherwise, we set $\Delta_{li} = 0$ and disregard the energy dependence of Γ_i ; in all cases the branching ratio, $\Gamma_{c,i}/\Gamma_i$, was assumed to be energy independent.

We will use Eq. (25) as an operational definition of the apparent “emission temperature” T ; this definition is useful to characterize the excitation energy densities of both equilibrium and nonequilibrium systems. It should be stressed, however, that the (unknown) effects of feeding from higher lying states are ignored. With this definition, one can only expect to measure the temperature of the emitting system if it is significantly smaller than the energy separation of the states investigated.²⁷ The use of the Maxwell-Boltzmann factor should be understood as part of this operational definition. Maxwell-Boltzmann distri-

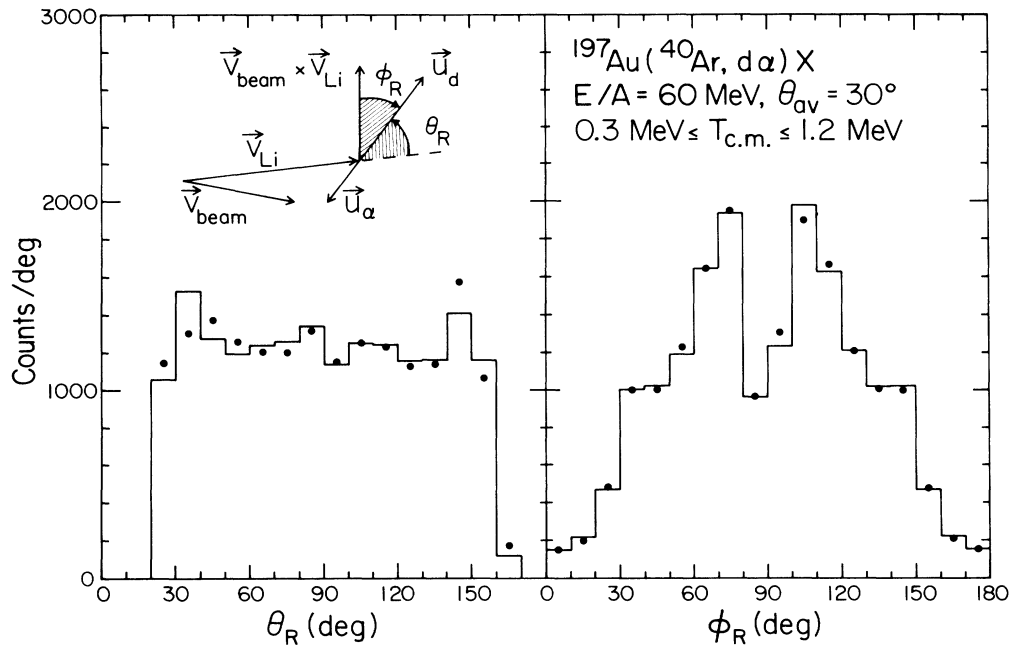


FIG. 23. Angular distributions of the decay yields from the first particle-unstable state in ${}^6\text{Li}$. The angles θ_R and ϕ_R are defined in the text and depicted in the inset. The histograms are results of Monte Carlo calculations assuming isotropic decay of the ${}^6\text{Li}$ nuclei.

butions can be used if $\exp(\mu/T) \ll 1$, where μ is the chemical potential (see Ref. 61, pp. 162ff). Quantum statistical model calculations⁸⁰ indicate that $\exp(\mu/T) \leq 0.05$ for the range of particles, breakup densities, and emission temperatures of interest.

In Fig. 20 the experimental yields are compared to calculations based on Eq. (25) for a variety of emission temperatures. The sum in Eq. (25) included the three $T=0$ excited states of ${}^6\text{Li}$ below 10 MeV excitation energy.⁶⁵ The calculations were normalized to reproduce the experimental yield over the energy range of $T_{c.m.} = 0.3\text{--}1.2$ MeV. For the quantitative determination of the mean emission temperature, we have integrated the decay yields over the energy ranges of $T_{c.m.} = 0.2\text{--}1.5$ and $1.5\text{--}5.0$ MeV and compared the ratio of these yields to the corresponding ratios calculated from Eq. (25). The value extracted from the relative populations of particle unbound states of ${}^6\text{Li}$ is $T = 4.8 \pm 1.2$ MeV.

We also investigated the relative population between the 2.186 MeV state in ${}^6\text{Li}$ and particle-stable ${}^6\text{Li}$ nuclei (ground state + 3.563 MeV state). If one ignored the complications resulting from the sequential decay of higher lying states, the (efficiency corrected) ratio of the experimental cross sections, $\sigma({}^6\text{Li}_{g.s.})/\sigma({}^6\text{Li}_{2.186}) = 0.8 \pm 0.2$, would indicate an apparent temperature of $T = 2.2 \pm 0.7$ MeV. (For the discussion of the complications which arise from sequential feeding from higher lying states, see Sec. VI.)

The experimental $t\text{-}\alpha$ coincidence yield resulting from the particle decay of excited ${}^7\text{Li}$ nuclei is shown in Fig. 24 as a function of excitation energy above particle threshold, $T_{c.m.}$. Due to uncertainties of the background correlation function below $q \leq 50$ MeV/c (see Fig. 9), the spectral shape below $T_{c.m.} \leq 1$ MeV is not well established; the error bars in the figure represent only statistical uncertain-

ties. For our calculations, we adopted the level scheme of Ref. 68; the locations of particle unstable states are indicated by arrows. Because of the large widths of the higher lying states, the calculations took penetrability effects into account; level parameters and branching ratios were taken from Ref. 65 for the two particle unstable

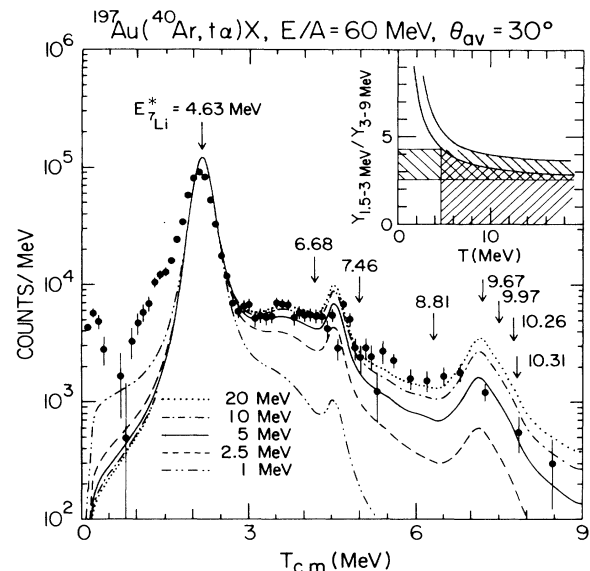


FIG. 24. Energy spectrum resulting from the decay of particle-unstable states in ${}^7\text{Li}$. Positions of states in ${}^7\text{Li}$ are marked by the arrows. The curves correspond to thermal distributions, Eq. (25), for $T = 1, 2.5, 5, 10,$ and 20 MeV. Inset: Calculated ratios of the integrated yields between $1.5\text{--}3$ MeV and $3\text{--}9$ MeV as a function of the temperature. The hatched area indicates the range of values consistent with the experimental spectrum.

states below the neutron emission threshold and from Ref. 68 for the remaining levels. The calculations were normalized to the experimental yield in the energy range $T_{c.m.} = 1.5\text{--}3.0$ MeV. Although the calculations describe the overall shape of the excitation spectrum, the predicted peaks due to the 7.46 and 9.67 MeV states are not observed experimentally. The broad shoulder observed at $T_{c.m.} \approx 1.5$ MeV might be an indication, that additional two-step decays,⁸¹ e.g., ${}^8\text{Li}^* \rightarrow t + {}^5\text{He} \rightarrow t + \alpha + n$, or Coulomb distortions affect the t - α coincidence cross section. An extrapolation of the bump at $T_{c.m.} \approx 1\text{--}1.5$ MeV indicates that up to 20% of the yield in the region of the 4.63 MeV state may be due to this background. (Misidentified d - α coincidences contribute less than 300 counts/MeV to the coincidence yield for $T_{c.m.} < 4$ MeV. For higher $T_{c.m.}$ values this contamination is negligible.)

In order to determine the apparent emission temperature of ${}^7\text{Li}$, we have integrated the decay yields over the energy ranges of $T_{c.m.} = 1.5\text{--}3.0$ and $3.0\text{--}9.0$ MeV. In the inset of Fig. 24 we compare this ratio to the ratio calculated as a function of temperature. Estimated uncertainties of these calculations due to insufficient information about the line shapes correspond to the band between the two solid curves. Within the experimental uncertainties (hatched region), we can only establish a lower limit of $T \geq 4.5$ MeV.

One can extract an emission temperature from the population ratio $\sigma_2/\sigma_0 = 0.29 \pm 0.05$, where σ_0 denotes the integrated cross section for particle-stable ${}^7\text{Li}$ nuclei (ground state + 0.478 MeV state) and σ_2 denotes the integrated cross section of ${}^7\text{Li}$ nuclei emitted in the 4.63 MeV state. [The integrated yield of stable ${}^7\text{Li}$ nuclei has been corrected for a $(1.5 \pm 0.5)\%$ contamination due to the pileup of two coincident α particles arising from the decay of ${}^8\text{Be}$ nuclei in their ground states;⁸² the calculation of this background is a trivial by-product of the calculations described in Sec. IV E.] If one ignored the feeding of the ${}^7\text{Li}$ ground state through sequential decay, this ratio would indicate an apparent temperature of $T = 2.9^{+0.4}_{-0.3}$ MeV. The quoted errors do not include the uncertainty from a possible background in the region of the 4.63 MeV state; a 20% background would reduce the apparent temperature by about 0.4 MeV.

We give a final example for the relative populations of states with level separations which are small as compared to temperatures of about 5 MeV by integrating the cross sections resulting from the α - ${}^7\text{Li}$ decay of particle unstable nuclei over the regions $q = 35\text{--}68$ and $68\text{--}100$ MeV/ c (Fig. 12). These regions are populated by known⁶⁵ states at 9.185 and 9.2744 MeV and 9.876, 10.26, 10.33, and 10.597 MeV, respectively. From the ratios of the cross sections,

$$\sigma(35\text{--}68 \text{ MeV}/c)/\sigma(68\text{--}100 \text{ MeV}/c) = 1.7 \pm 0.4,$$

we obtain a lower limit $T \geq 4.5$ MeV. Because of a lack of spectroscopic information, this analysis did not include possible contributions from higher lying broad states; we estimate that such contributions could reduce this limit by as much as 2 MeV. Because of the small level spacing, this temperature determination is less meaningful.

The apparent emission temperatures are sensitive to dis-

tortions of the primary population ratios whenever the level separations are smaller or comparable in magnitude to the actual temperature.²⁷ More accurate determinations of the emission temperatures can be made from the relative populations of widely separated states. Suitable decays of such highly excited states exist in ${}^4\text{He}$, ${}^5\text{Li}$, and ${}^8\text{Be}$ nuclei.

To determine the emission temperature of ${}^8\text{Be}$, the decay yields were integrated over the range of excitation energy for which the coincidence yields are dominated by the decay of the 3.04 MeV state in the α - α channel [Fig. 11(a)] and the 17.64 MeV state in the p - ${}^7\text{Li}$ channel [Fig. 11(b)]. The corresponding integrals were performed for the calculated decay yields. For the efficiency calculations, the energy and angular distributions of the ${}^8\text{Be}$ parent nuclei were parametrized in terms of simple moving sources, Eq. (3). Except for a 30% higher Coulomb repulsion, the parameters were chosen to be identical to those which fit the cross sections of stable ${}^7\text{Li}$ nuclei; see Table III. For the spectral distribution in the α - α channel, the ${}^8\text{Be}$ ground state, the 3.04 MeV state and the broad 11.4 MeV state were included in the sum of Eq. (25). Level parameters were taken from Ref. 73; they include penetrability effects. The calculations of the emission spectrum in the p - ${}^7\text{Li}$ channel covered the 17.64 MeV state, the 18.15 MeV state ($\Gamma_p/\Gamma = 1.00$), and the 18.91, 19.07, 19.24, and 19.4 MeV levels ($\Gamma_p/\Gamma = 0.5, 1.0, 0.5$, and 0.5 ; see Ref. 83). They included a 4% decay probability⁶⁵ of the 18.15 MeV state to the first excited state in ${}^7\text{Li}$ at 0.478 MeV which contaminates the peak at 17.64 MeV; see Fig. 11(b).

The functional dependence of the calculated yield ratio N_L/N_H is shown by the solid line in the right-hand part of Fig. 25. Here, N_L and N_H denote the integrated yields of the states at lower and higher excitation energy, respectively. The hatched region in the figure indicates the range of yield ratios and temperatures which are consistent with the extreme background assumptions shown in Fig. 11. Statistical errors or errors introduced by un-

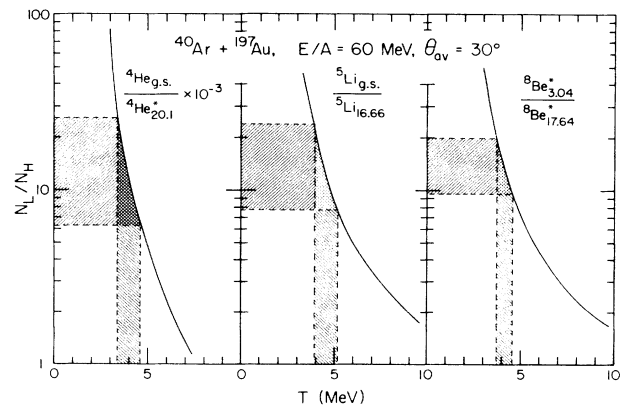


FIG. 25. Yield ratios N_L/N_H corresponding to states in ${}^4\text{He}$, ${}^5\text{Li}$, and ${}^8\text{Be}$. The solid curves show the calculated ratios as a function of the emission temperature. The hatched regions indicate the range of values consistent with our assumptions for the background correlation functions in Figs. 4, 7, and 11.

certainties in the Monte Carlo calculations are insignificant. Variations of the source parameters [T_i and E_i in Eq. (3)] of the ${}^8\text{Be}$ parent nuclei by 30% change the calculated yield ratios by less than 5% and the extracted temperature by about 0.1 MeV. The relative populations of the 3.04 and the 17.64 MeV states in ${}^8\text{Be}$ indicate an emission temperature of $T=4.2\pm 0.5$ MeV. Because of the large energy spacing between the two levels, significantly different emission temperatures can be excluded.

For the sake of completeness, we also extracted the yields of ${}^8\text{Be}_{g.s.}$. It was assumed that the main peak of the ${}^8\text{Be}$ ground state [located at $q\leq 30$ MeV/c; see Fig. 11(a)] contains 95% of the total ground state strength; the remaining 5% were assumed to be distributed over the ghost state;⁷³ see Sec. IV E. The deduced population ratio $\sigma_1/\sigma_0=1.15\pm 0.50$ between the 3.04 MeV state and the ground state corresponds to an apparent emission temperature of 2.0 ± 0.7 MeV, indicating the importance of sequential decay processes.

In order to extract an emission temperature for ${}^5\text{Li}$, we investigated the population of the ${}^5\text{Li}$ ground and 16.66 MeV states which decay via the p- α [Fig. 7(a)] and the d- ${}^3\text{He}$ [Fig. 7(b)] channels, respectively. For the description of the line shape of the ground state, R -matrix parameters from Ref. 77 were used. Because of the vicinity of the particle threshold to the 16.66 MeV state, level parameters from Ref. 65 were used to take care of penetrability effects. As before, the experimental and calculated decay yields were integrated over energy ranges dominated by the relevant states ($22\leq q_{p-\alpha}\leq 100$ MeV/c and $10\leq q_{d-{}^3\text{He}}\leq 50$ MeV/c). The background correlation functions were assumed to lie within limits given by the dashed lines in Fig. 7.

Contaminations from misidentified d- α pairs resulting from decays of ${}^6\text{Li}^*$ were estimated to be less than 10%. The relative populations of the two widely separated states in ${}^5\text{Li}$ are shown in the center part of Fig. 25; they indicate emission temperatures of $T=4.6\pm 0.7$ MeV.

The emission temperature of ${}^4\text{He}$ nuclei was determined from the population of the well known state at 20.1 MeV ($q\leq 30$ MeV/c, Fig. 4) and the total yield of α particles. Energy and angular distributions of particle unstable ${}^4\text{He}$ nuclei were assumed to be identical to those of particle stable alpha particles. The calculation of the excitation energy spectrum included the states at 20.1, 21.1, and 22.1 MeV. Penetrability effects were included by means of the level parameters given in Ref. 64. The calculated temperature dependence of the decay yields is shown by the solid line in the left-hand part of Fig. 25; the extracted emission temperatures is $T=4.2^{+0.5}_{-0.7}$ MeV. We have presented several examples of the feeding of α particles by the decay of unstable nuclei (e.g., ${}^5\text{Li}$, ${}^6\text{Li}^*$, ${}^7\text{Li}^*$, and ${}^8\text{Be}$). Because of the large level separation, $\Delta E/T\approx 5$, the extracted temperature is less sensitive to the effects of sequential feeding: a 50% variation of the primary population ratio changes the apparent temperature by less than 1 MeV.

The energy averaged apparent emission temperatures discussed in this subsection are summarized in Fig. 26. Temperatures between 4 and 5 MeV were extracted from the relative population of two widely separated levels or

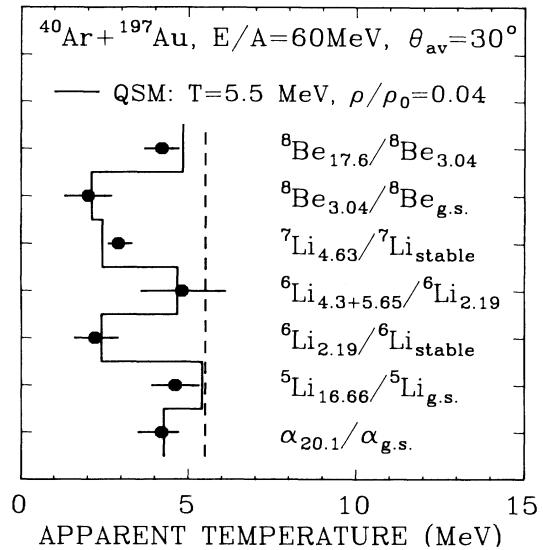


FIG. 26. Apparent emission temperatures for ${}^{40}\text{Ar}$ induced reactions on ${}^{197}\text{Au}$ at $E/A=60$ MeV. The histogram shows the results of a quantum statistical calculation which includes the feeding by sequential decay; an initial temperature of $T=5.5$ MeV and a density of $\rho/\rho_0=0.04$ were assumed.

two excited states. On the other hand, significantly lower temperatures were deduced from the relative populations of the ground state and a low lying excited state. Different temperatures for the same nucleus (see ${}^6\text{Li}$ and ${}^8\text{Be}$) could be due to the breakdown of the assumption of local statistical equilibrium for the primary emission process or, alternatively, due to perturbations of the primary distributions after emission from the reaction zone. We will discuss the effects of sequential decays more quantitatively in Sec. VI.

C. Energy dependence of emission temperatures

In this section we discuss the dependence of the relative populations of excited states on the kinetic energy of the detected particles. Figure 27 shows the α - α and p- ${}^7\text{Li}$ correlation functions for different constraints on the summed kinetic energy, E_1+E_2 , of the two coincident particles. The gates are indicated in the figure. The normalization constants C_{12} , Eq. (4), are identical to those used for the correlations shown in Figs. 11(a) and 11(b), respectively. For the extraction of the emission temperatures we used the states at 3.04 MeV ($65\leq q\leq 140$ MeV/c) and 17.64 MeV ($18\leq q< 32$ MeV/c). In addition, we extracted the population of the 18.15 MeV state in the range $32\leq q\leq 45$ MeV/c. The same constraints on the kinetic energies and relative momenta of the coincident particles were used in the Monte Carlo calculations which determine the theoretical yields as a function of temperature. The energy dependence of the relative populations of $\alpha_{g.s.}$, $\alpha_{20.1}^*$, ${}^5\text{Li}_{g.s.}$, and ${}^5\text{Li}_{16.66}$ was determined in a similar fashion.

The dependence of the extracted emission temperatures on the total kinetic energy per nucleon, $(E_1+E_2)/(A_1+A_2)$, is shown in Fig. 28. The horizontal

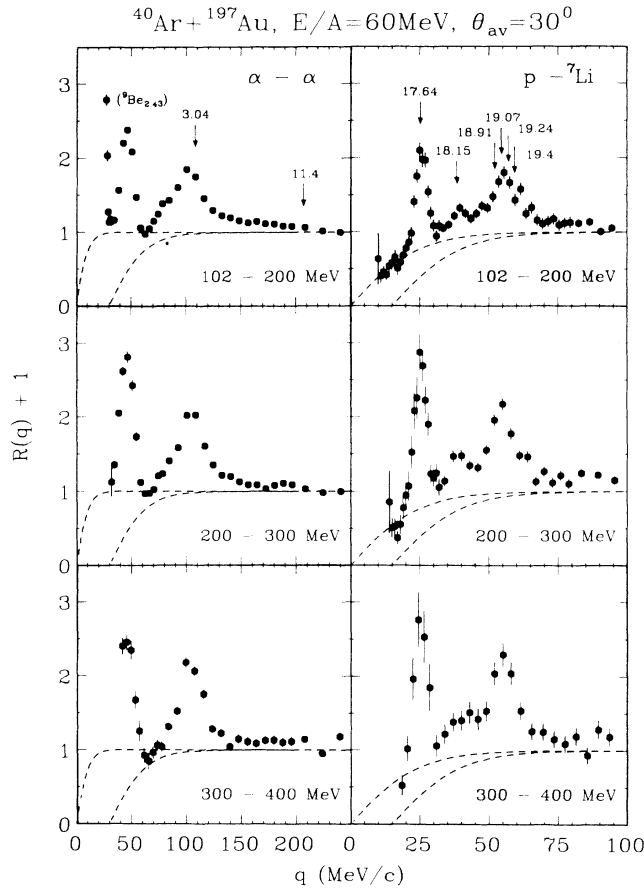


FIG. 27. Correlation functions measured for two coincident alpha particles (left-hand panel) and coincident protons and ${}^7\text{Li}$ nuclei (right-hand panel) for different constraints on the total kinetic energy, $E_1 + E_2$. The dashed lines show the limits for the background correlation functions used to extract the decay yields. Locations of excited states in ${}^8\text{Be}$ are marked by the arrows.

dashed lines indicate the energy range over which the population yields were integrated. The vertical error bars reflect uncertainties in the choice of the background correlation function. The errors for different energy cuts are not completely uncorrelated, since the background functions for different energy cuts are not independent of each other. Statistical uncertainties are of the order of $\Delta T \leq 0.5$ MeV. No clear energy dependence of the emission temperature can be established from the present data.

For the case of ${}^{14}\text{N}$ induced reactions on ${}^{197}\text{Au}$ at $E/A = 35$ MeV, the relative populations of particle unstable states in ${}^6\text{Li}^*$ nuclei indicated⁴⁸ higher emission temperatures for higher particle energies, $E_\alpha + E_d$. For the present reaction, we do not find such an energy dependence. Within experimental errors, the relative populations of states in ${}^6\text{Li}^*$ are consistent with an emission temperature of $T \approx 4.5$ MeV, independent of the energy of the emitted particles.

An energy dependence of the level populations can be caused by energy dependent contributions from sequential feeding. Such effects were already discussed in the litera-

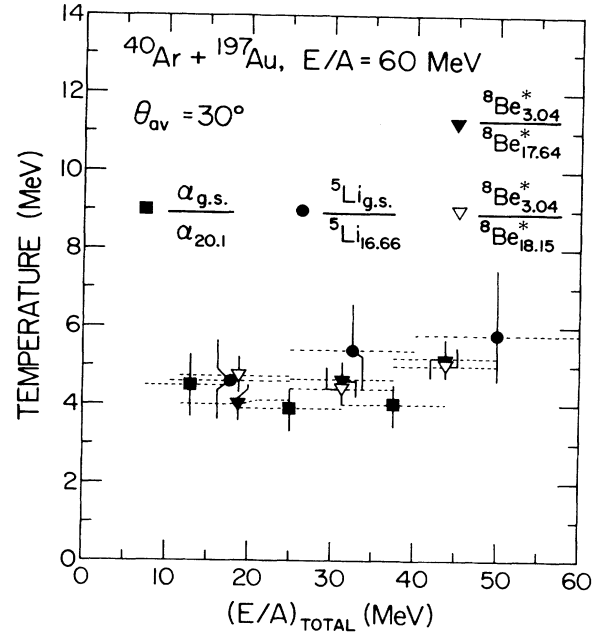


FIG. 28. Apparent emission temperatures from the relative populations of widely separated states in ${}^4\text{He}$, ${}^5\text{Li}$, and ${}^8\text{Be}$ as a function of the total kinetic energy per nucleon, $(E_1 + E_2)/(A_1 + A_2)$. The horizontal dashed lines indicate the range over which the coincidence yields were summed to obtain the population of states.

ture for the explanation of the low energy portions of the kinetic energy spectra³³ and of the different slopes of the energy spectra of pions and protons emitted in high energy nucleus-nucleus collisions.⁸⁴ The effect is illustrated in Fig. 29. Here, inclusive deuteron kinetic energy spectra are compared to the spectra of deuterons which originate from the sequential decay of particle unstable ${}^6\text{Li}$ nuclei. Deuterons produced via the sequential decay of heavier, particle unstable fragments have lower kinetic energies because their kinetic energy spectra are dominated by the lower velocities of the heavier parent nuclei. As a consequence, contaminations from sequential decays may be particularly serious at low kinetic energies. The ratio of the deuteron spectrum due to the decay of ${}^6\text{Li}^*$ and the inclusive spectrum illustrates this point very clearly; see upper part of Fig. 29.

VI. SEQUENTIAL DECAY

A. Feeding from sequential decays

We determined the contributions from decays of particle unstable fragments, by inverting Eq. (24). In cases where the integrated efficiency, $\hat{\epsilon}(E) = \int \epsilon(E', E) dE'$, or the excitation spectrum, $dn(E)/dE$, varied only little over a region δE of the order of the hodoscope resolution, we approximated the total sequential feeding, $\langle d\sigma/d\Omega \rangle_c$, resulting from the decay channel $c \rightarrow 1 + 2$ by

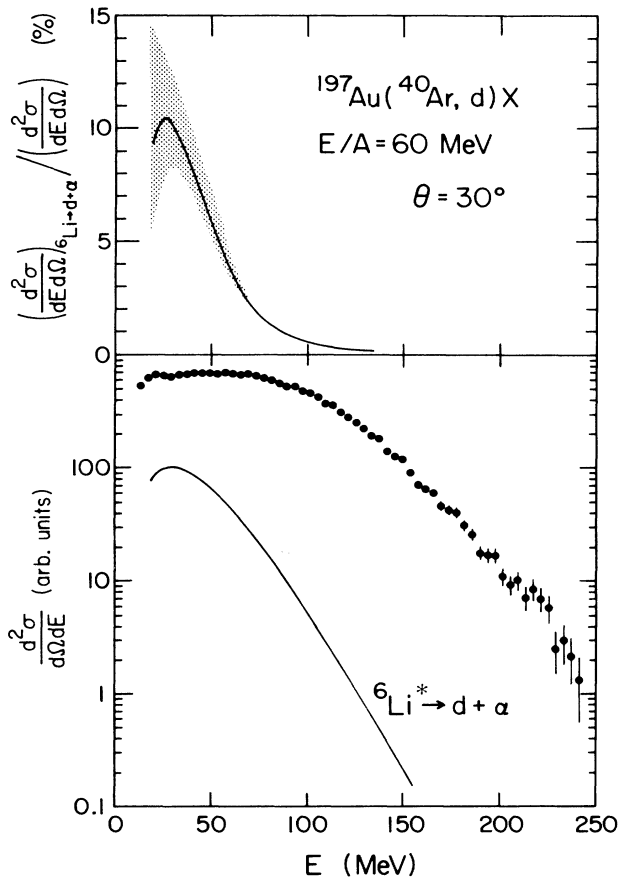


FIG. 29. Lower panel: Single particle cross section for deuterons at a laboratory angle of $\theta = 30^\circ$ (solid points) and contribution to the inclusive deuteron cross section from the decay of particle unstable states in ${}^6\text{Li}$ (solid line) as a function of the deuteron energy. In the upper part the ratio of these two cross sections is shown. The shaded area indicates the experimental uncertainties.

$$\begin{aligned} \left\langle \frac{d\sigma}{d\Omega} \right\rangle_c &= \frac{1}{1-f} \int dE \left[\frac{dn(E)}{dE} \right]_c \\ &\approx \frac{1}{1-f} \int dT_{c.m.} Y_c(T_{c.m.}) / \hat{\epsilon}(T_{c.m.}) \end{aligned} \quad (26)$$

Here, f denotes the fraction of the cross section which has not been detected due to the low energy cuts in the kinetic energy distributions. Moving source parametrizations (Table III) were used to determine this efficiency factor; typically, f was of the order of 0.1. The integral in Eq. (26) was performed over the range of relative energies which showed clear contributions from sequential decay. For narrow states (e.g., ${}^8\text{Be}_{g.s.}$), Eq. (24) was solved by an iterative procedure. Uncertainties involved with these evaluations were estimated to be less than 5%. Main errors are due to uncertainties of the background correlation functions and extrapolations of the kinetic energy distributions to low energies.

We have also extracted the contributions from the de-

cay ${}^4\text{Li} \rightarrow p + {}^3\text{He}$, which was not used for the extraction of an emission temperature. Figure 30 shows the efficiency corrected emission spectrum of ${}^4\text{Li} \rightarrow p + {}^3\text{He}$. Open and solid points correspond to the extreme background correlation functions (see dashed lines in Fig. 6). Excitation energy spectra for thermally emitted ${}^4\text{Li}$ nuclei are given by the lines. For these calculations level parameters from Ref. 67 were used for the four overlapping states in ${}^4\text{Li}$. The calculations were normalized to the average integral of the experimental spectrum. (Although we cannot establish an emission temperature from the data, the shape of the experimental emission spectrum is not inconsistent with a thermal distribution with $T \approx 5$ MeV.)

The relative contributions, $\langle d\sigma/d\Omega \rangle_{Y \rightarrow A+B} / \langle d\sigma/d\Omega \rangle_A$, from the various measured decay channels are summarized in Fig. 31. In some instances, more than 10% of the inclusive cross section of a particle stable nucleus can be traced back to a single decay channel: about 16% of all stable ${}^7\text{Li}$ nuclei originate from decays of excited ${}^{11}\text{B}$ nuclei. Figure 32 shows the relative feeding of nucleus A , summed over all experimentally observed channels. Between 10% and 30% of the inclusive yield of stable hydrogen and helium isotopes and ${}^7\text{Li}$ is generated in secondary decay processes in which two charged particles are emitted. Quantitative descriptions of particle emission from highly excited nuclear systems must address the important questions of secondary decays.

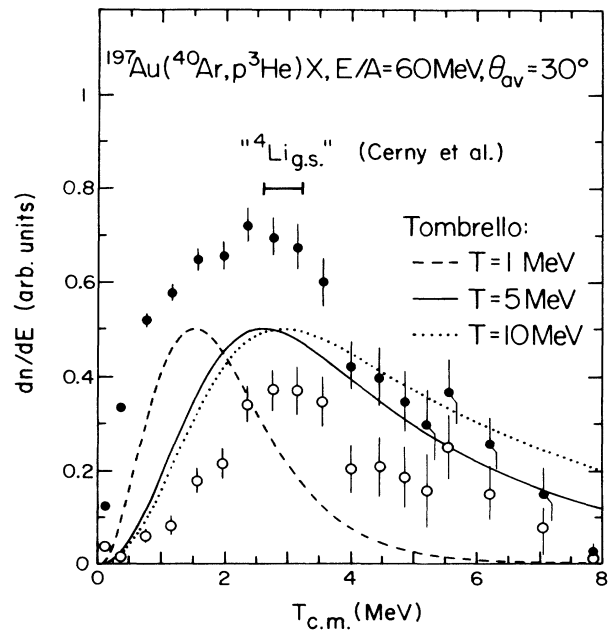


FIG. 30. Emission spectrum of (${}^4\text{Li} \rightarrow p + {}^3\text{He}$) as a function of relative energy after correcting the decay yield for the efficiency of the hodoscope. The open and solid symbols correspond to the two extreme background correlation functions in Fig. 6. The location of the ground state of ${}^4\text{Li}$ and its uncertainty are indicated by the horizontal bar. The dashed, solid, and dotted lines represent emission spectra of ${}^4\text{Li}$ for different temperatures using the level parameters of Ref. 67.

B. Quantum statistical model calculations

Our measurements provide only limited information about the decays of primary nuclei with $A > 8$; more importantly, we have no experimental information about neutron decays. In order to assess the importance of sequential decay processes in a more quantitative fashion and evaluate the resulting uncertainties for the deduced emission temperatures, we performed calculations with the quantum statistical model of Hahn and Stöcker.⁸⁰

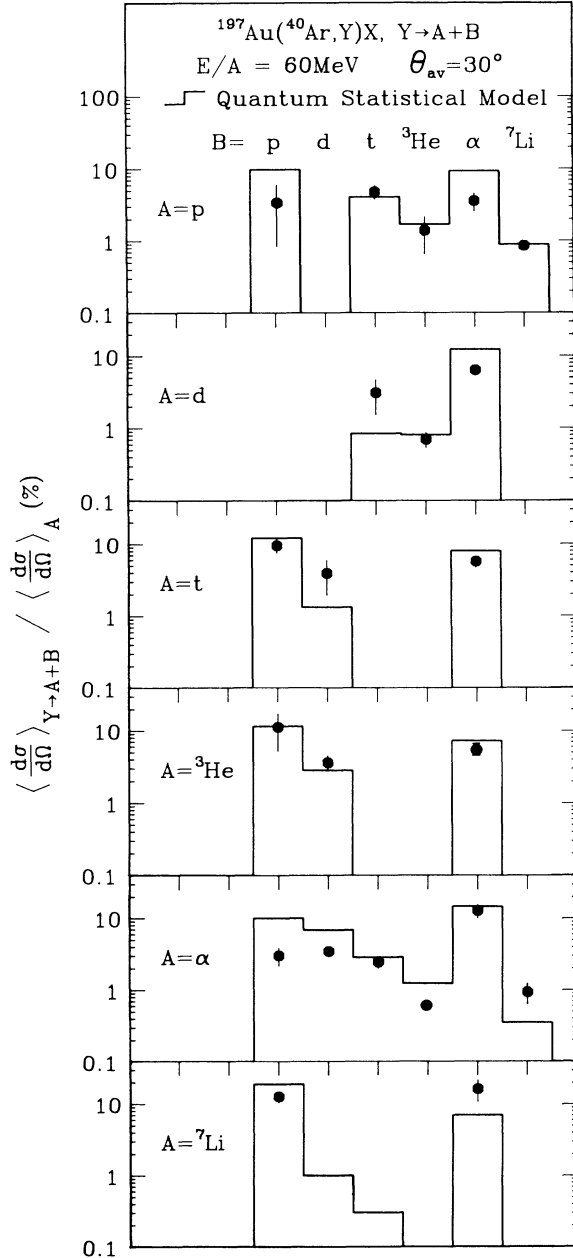


FIG. 31. Relative contributions to the average single particle inclusive cross sections of particle A from the decay channel $Y \rightarrow A+B$. The histograms show calculations with the quantum statistical model using $\rho/\rho_0=0.04$ and $T=5.5$ MeV.

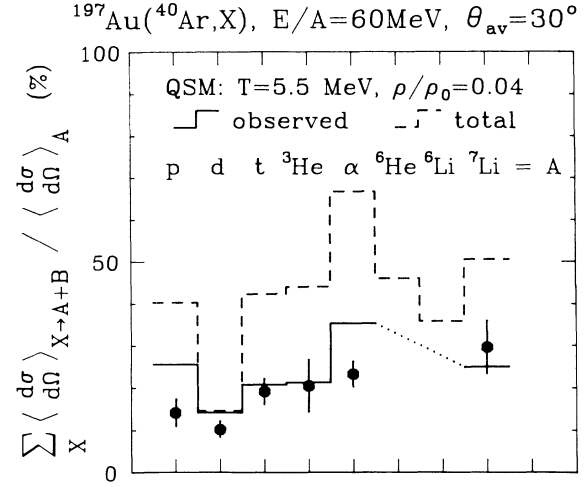


FIG. 32. Relative feeding of the inclusive cross section of nucleus A at $\theta_{av}=30^\circ$ summed over measured decay channels. The solid histogram represents the fit to the data by the quantum statistical model. The dashed histogram indicates the total feeding predicted by the quantum statistical model; neutron decays account for the major part of the missing yield.

The calculations proceed in two stages. In the first stage the relative population of stable and unstable states are calculated assuming an infinite system in chemical equilibrium which is characterized by a temperature T , a uniform density ρ , and a neutron-to-proton ratio (N/Z). Only known⁶⁵ asymptotic states are taken into consideration. In the subsequent stage, the excited states decay statistically to stable or long-lived ($\tau \geq 100$ ns) final nuclei which are detected experimentally. Whenever possible, the sequential decays were determined using existing spectroscopic information⁶⁵ concerning spins and branching ratios.

In order to determine the parameters T , ρ , and N/Z , we performed a χ^2 -minimizing fit to the measured population ratios (expressed in terms of apparent emission temperatures, Fig. 26), the relative feeding contributions via the various decay channels (Fig. 31), and the averaged yields of stable fragments (p, d, t, ^3He , α , ^6He , ^6Li , and ^7Li) and unstable nuclei in their ground states (Fig. 33). The calculations were found to be rather insensitive to the neutron-to-proton ratio. Variations of N/Z between $(N/Z)_{\text{Ar}} \approx 1.2$ and $(N/Z)_{\text{Au}} \approx 1.5$ changed the final results by less than 10%. For the calculations presented here, we fixed the neutron-to-proton ratio at a value $N/Z=1.35$, assuming equal contributions from projectile and target.

Figure 34 shows a contour plot of the χ^2 per degree of freedom in the temperature-density plane. Generally, the calculations are more sensitive to the breakup temperature than to the breakup density. Temperatures lower than about 4 MeV are clearly excluded; on the other hand, the χ^2 distribution rises rather slowly for temperatures, $T \geq 6$ MeV. If one fits only population ratios and relative feeding contributions and disregards the inclusive cross sections, the χ^2 distribution increases more steeply towards higher temperatures and clearly constrains the tempera-

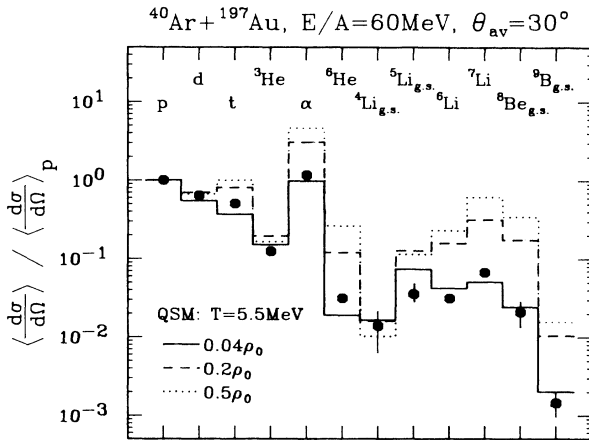


FIG. 33. Average single particle inclusive cross sections at $\theta_{av}=30^\circ$ for stable fragments relative to the proton cross section. The histograms show calculations with the quantum statistical model using $T=5.5$ MeV and $\rho/\rho_0=0.04, 0.2,$ and 0.5 .

ture to a value of about 5 MeV. Since we are interested in the absolute contributions by sequential decay, we require an approximate description of the single particle inclusive cross sections; see Fig. 33. The best agreement with our data was obtained with a breakup density of $\rho/\rho_0=0.04$ and $T=5.5$ MeV. Results of this best fit are shown as histograms in Figs. 26, 31, and 33.

In Fig. 35 the calculations are compared to the relative cross sections of complex particles, $A \leq 14$, measured for

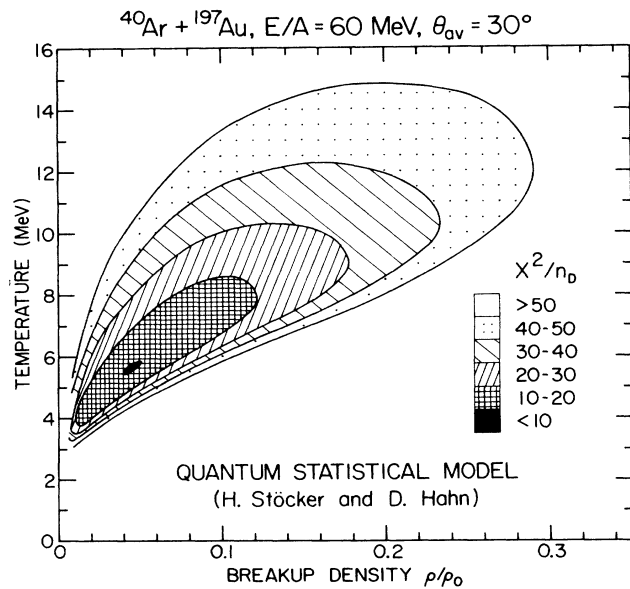


FIG. 34. Contours of constant χ^2 per degree of freedom in the density-temperature plane for fits with the quantum statistical model to the observed population ratios, relative feeding contributions, and single particle inclusive cross sections using $N/Z=1.35$.

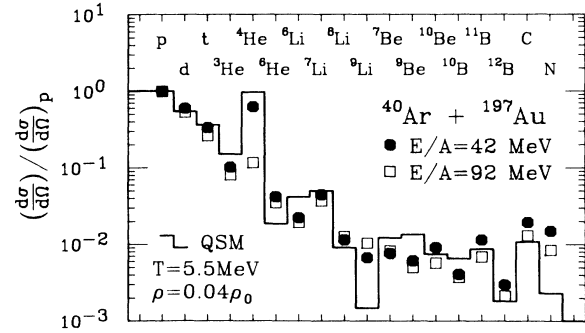


FIG. 35. Heavy fragment yields observed (Ref. 18) in the reaction $^{40}\text{Ar} + ^{197}\text{Au}$ at $E/A=42$ and 92 MeV. The histogram shows predictions of the quantum statistical model using $T=5.5$ MeV, $\rho/\rho_0=0.04$, and $N/Z=1.35$.

^{40}Ar induced reactions on ^{197}Au at $E/A=42$ and 92 MeV.¹⁸ The agreement is good. For the present experiment the calculated feeding from all decay channels is shown by the dashed histogram in Fig. 32. The model predicts that up to 50% of the inclusive light fragment yields may be due to the sequential decay of highly excited primary reaction products. The inclusion of sequential decay processes can also explain the variation of the apparent emission temperatures extracted via Eq. (25). In Fig. 26 the solid histogram shows the apparent emission temperatures, defined in terms of Eq. (25) from the final population ratios, which are predicted by the quantum statistical model for a system of uniform temperature $T=5.5$ MeV and density $\rho=0.04\rho_0$. The agreement with the measured values is striking. Low apparent temperatures are observed and predicted for population ratios for which a particle stable ground state is compared to a low lying excited state. These low apparent temperatures are quantitatively understood in terms of the sequential feeding from particle unstable primary fragments.

Surprisingly low emission temperatures of $T \approx 0.3-0.5$ MeV were recently extracted from the populations of low lying particle stable states in ^7Li , ^8Li , and ^7Be which decay by γ emission.^{26,28} The quantum statistical model predicts population ratios for the ground and first excited states in ^7Li , ^7Be , and ^8Li which correspond to apparent "emission temperatures" of 0.5, 0.6, and 1.2 MeV, respectively, when no corrections for sequential feeding are made. The calculations suggest that the population ratios of these states are dominated by sequential feeding from higher lying states and that they are rather insensitive to the temperature of the emitting system once it exceeds about 2–3 MeV; also see Ref. 36.

The extracted breakup density, $\rho_{bu} \approx 0.04\rho_0$, is considerably smaller than commonly accepted values,^{13,44,85,86} $\rho_{bu} \approx (0.25-0.5)\rho_0$. Whether such a low breakup density can be reconciled with the basic assumption of chemical and thermal equilibrium at the point of freeze-out will require further detailed theoretical investigations. Estimates of hadronic reaction rates during the disassembly phase³⁵ indicate that rearrangement collisions may play an important role up to densities as low as $\frac{1}{20}\rho_0$. On the oth-

er hand, the entropy per nucleon extracted from the model fit, $S/A=2.8$, is in the range of other experimental observations.^{18,87}

During the later stages of the reaction, the system is expected to expand nearly isentropically. The entropy is predicted^{88,89} to increase by about $\Delta S/A \approx 0.3-0.6$. If the reaction trajectory passes through the region of mechanical instability, the entropy might increase^{90,91} by an additional amount of $\Delta S/A \approx 0.5-1.0$. In order to estimate the breakup density, ρ_f , one may use the relation between temperature, density, and entropy for a Maxwell-Boltzmann gas (Ref. 61, pp. 125ff),

$$\rho_f/\rho_i = (T_f/T_i)^{3/2} e^{-\Delta S/A}. \quad (27)$$

For $T_i \approx 16$ MeV, $\rho_i = \rho_0$, and $\Delta S/A = 1.2$, one obtains a breakup density of $\rho_f = \rho_{bu} \approx 0.06\rho_0$. This value is consistent with the breakup density which has been deduced from the quantum statistical model calculations. If, on the other hand, the expansion is nearly adiabatic, one would obtain $\rho_f \approx 0.2\rho_0$.

Clearly, one cannot expect agreement in every detail. Both the calculation of the primary distribution and of the sequential decay involve considerable uncertainties. Only known states with their asymptotic spectroscopic parameters were included and possible in-medium effects were neglected. Another outstanding problem concerns the consistent treatment of the nuclear continuum and the timescales of emission. Qualitatively, the inclusion of additional states will increase contributions from sequential feeding. Inertial effects (which have received increasing attention for the case of low energy fission^{92,93}) are completely neglected; such effects may play a decisive role during the expansion phase of the system.

Within statistical evaporation models,^{22,33} the fragment yields are strongly influenced by the Coulomb barrier of the emitting nucleus.²⁴ Since the quantum statistical calculations are based on the assumption of infinite nuclear matter, Coulomb barrier penetrabilities are not incorporated. In this model, the relative fragment yields depend strongly on the breakup density; see Fig. 33. (Both approaches are, of course, sensitive to binding energies.) However, Coulomb barrier penetrabilities must clearly be important for finite nuclei and their neglect could be a serious deficiency of the quantum statistical model. In fact, quantum statistical calculations predict too large yields for proton-rich isotopes (e.g., ²He and ⁵Li) and too small yields for neutron-rich isotopes (e.g., ⁵He). This discrepancy remains even if the N/Z ratio is increased to 1.5 and could be due to the neglect of Coulomb barrier effects.

Considerable uncertainties remain for the treatment of the sequential decay problem because of limited spectroscopic information for many of the included states. The present calculations⁸⁰ may be expected to provide a reasonable treatment of the *average* decay properties of the system even when the spins or branching ratios of particular states are not known. (This was checked by using statistical decay parameters for *all* states and comparing the results to calculations for which all known experimental information was used.) Since nuclear structure effects dominate the decay properties of many light nuclei, con-

siderable uncertainties may exist for specific states.

Improvements of the experimental techniques are also desirable. Our measurements do not select specific ranges of impact parameters or specific classes of reactions. Up to now, measurements exist only over a limited range of angles. It remains to be investigated, whether different reaction mechanisms are associated with different primary distributions.

With these reservations in mind, we may summarize that our data are rather well described by an equilibrium model. Each resonance which could be detected by our apparatus was, indeed, observed experimentally. Of course, these findings do *not* constitute a proof for the establishment of local equilibrium in intermediate energy nuclear collisions. They do, however, indicate that statistical approaches provide a useful tool for the understanding of these reactions for which large portions of the available phase space appear to be populated. The incorporation of dynamical and nonequilibrium statistical aspects in a consistent theoretical framework remains a challenging problem.

VII. DISCUSSION AND SUMMARY

In this paper we have presented a detailed investigation of two-particle correlations at small relative momenta for the reaction ⁴⁰Ar + ¹⁹⁷Au at $E/A=60$ MeV. The sensitivity of the correlation functions to final-state interactions of the emitted particles offers the possibility for a simultaneous study of the space-time distribution of the nuclear system and the source temperature at the point of emission.

The space-time extent of the emitting source was found to depend on the particle species and to decrease with increasing kinetic energies of the particle pairs. Particle pairs whose interactions are essentially nonresonant (d-d and t-t) show the largest source parameters. Particle pairs which experience resonant interactions exhibit significantly smaller source dimensions. A similar sequence of source radii was observed⁴⁵ for ¹⁴N induced reactions on ¹⁹⁷Au at $E/A=35$ MeV. The present observations might provide a first hint that different particle species decouple at different average densities. The observed energy dependence of the correlation functions might be caused by a collective radial expansion⁵⁰ of the interaction zone; alternatively, it might reflect the temporal evolution of the equilibrating system, indicating the emission of more energetic particles at earlier stages of the reaction. (Sequential decays of excited primary fragments may be considered as an extreme example for reactions which proceed via longer emission timescales.) More sophisticated theoretical treatments of two-particle correlations which include the temporal and dynamical aspects of the reaction are needed before these questions can be addressed quantitatively.

Most of the correlation functions discussed in this paper are dominated by resonant final-state interactions of the two coincident particles, i.e., by the emission of particle unstable nuclei. Sequential decay contributions to the inclusive spectra of the order of 20% were determined by integrating the measured yields from the decay of particle

unstable resonances. Quantum statistical model calculations were utilized to extrapolate to contributions from decay channels not measured in the present experiment. For certain particles, up to $\frac{1}{2}$ of the yield could be due to sequential feeding from particle unbound states.

Different apparent emission temperatures were extracted from the relative populations of different pairs of states when the effects of sequential feeding from higher lying particle unstable states were neglected. The inclusion of sequential feeding from particle unbound states within the quantum statistical model⁸⁰ made it possible to describe the measured level populations in terms of a thermal distribution characterized by a *common* temperature, $T=5.5$ MeV, and density, $\rho=0.04\rho_0$, at the point of emission. Whether such low densities are realistic or whether they are an artifact of the approximations of the model remains to be investigated in the future.

Whereas the extracted source radii depend on the summed kinetic energy of the coincident particles, no evidence was found for such an energy dependence of the relative level populations or emission temperatures. This observation is different from the results of Ref. 48, where smaller source radii *and* higher emission temperatures were extracted for more energetic α -d pairs.

The emission temperature, $T\approx 5.5$ MeV, is about a factor of 3 lower than the temperature parameter, $T_2\approx 16$ MeV, which characterizes the kinetic energy spectra at intermediate rapidities. This might be an indication that the degrees of freedom associated with the translational motion and the internal excitation go out of equilibrium at different stages of the reaction.³⁵ Furthermore, distortions of the kinetic energy spectra due to possible collective flow effects or due to the expansion of the system may render the extraction of temperatures from the kinetic energy spectra ambiguous, if not impossible. Fluid dynamical calculations^{21,88} indicate that the slope parameter of the kinetic energy spectra should be close to the *initial* temperature of the system even if collective flow sets in during the expansion phase of the reaction. Temperatures extracted from the relative populations of states, on the other hand, correspond to the temperature of the system at the point of emission. It remains to be investigated whether our observations can be understood quantitatively in terms of an expanding and cooling system. The ob-

served energy dependence of the source radii could be the signature of an (explosive) expansion of the system.^{48,50} It may, however, also reflect the temporal evolution of highly excited nuclear systems, since the timescales for particle emission are expected to increase as the system cools by particle emission.⁹⁴

Emission temperatures similar to the one extracted in this experiment have been inferred for several other systems. For ^{14}N induced reactions on ^{197}Au , mean emission temperatures of $T\approx 4-5$ MeV were extracted from the relative populations of particle unbound states in ^3Li and ^6Li nuclei.⁴⁸ Finite-temperature Hartree-Fock calculations have presented that excited nuclei should only exist below a "limiting temperature." This limiting temperature should depend on the mass of the excited nucleus; typical values are predicted to be of the order of $T\approx 5-10$ MeV.¹⁶ Limiting compound nucleus temperatures of the order of 5 MeV were inferred from the disappearance of fusion-like reactions at incident energies above $E/A\approx 30$ MeV.^{95,96} Temperatures of the order of 5 MeV were also deduced²³ from the relative abundances of heavy fragments observed in proton, carbon, and neon induced reactions in the energy range 1–300 GeV. Future experiments will have to clarify whether, indeed, the emission of complex fragments is limited to systems with temperatures below 5 MeV, or whether this value will find its ultimate explanation in extended chains of secondary and tertiary disintegration processes.

ACKNOWLEDGMENTS

We wish to thank Dr. D. Hahn and Prof. H. Stöcker for providing us with their quantum statistical model code. This article is based upon work supported by the National Science Foundation under Grants PHY-83-12245 and PHY-84-01845, by the Centre National de la Recherche Scientifique under Contract DRCI-AI No. 49.85.22., and by the Natural Sciences and Engineering Research Council of Canada. One of us (J. Po.) acknowledges the receipt of a fellowship of the Deutsche Forschungsgemeinschaft (Federal Republic of Germany). Another of us (W.G.L.) acknowledges the receipt of a Presidential Young Investigator Award.

*Present address: Institut für Kernphysik, Johann-Wolfgang-Goethe Universität, 6000 Frankfurt 90, Federal Republic of Germany.

†On leave from Université de Nantes, Nantes, France.

‡On leave from Hahn-Meitner-Institut für Kernforschung, Berlin, Federal Republic of Germany.

§Permanent address: Institute for Nuclear Research, Warsaw, Poland.

¹G. Bertsch, H. Kruse, and S. Das Gupta, Phys. Rev. C **29**, 673 (1984); J. Aichelin and G. Bertsch, Phys. Rev. C **31**, 1730 (1985).

²H. Kruse, B. V. Jacak, J. J. Molitoris, G. D. Westfall, and H. Stöcker, Phys. Rev. C **31**, 1770 (1985).

³B. Remaud, C. Grégoire, F. Sebillé, and L. Vinet, Phys. Lett. **180B**, 198 (1986).

⁴M. B. Tsang, R. M. Ronningen, G. Bertsch, Z. Chen, C. B. Chitwood, D. J. Fields, C. K. Gelbke, W. G. Lynch, T. Nayak, J. Pochodzalla, T. Shea, and W. Trautmann, Phys. Rev. Lett. **57**, 559 (1986).

⁵G. D. Westfall, J. Gosset, P. J. Johansen, A. M. Poskanzer, W. G. Meyer, H. H. Gutbrod, A. Sandoval, and R. Stock, Phys. Rev. Lett. **37**, 1202 (1976).

⁶J. Gosset, J. I. Kapusta, and G. D. Westfall, Phys. Rev. C **18**, 844 (1978).

⁷J. Knoll, Phys. Rev. C **20**, 773 (1979).

⁸W. A. Friedman and W. G. Lynch, Phys. Rev. C **28**, 950

- (1983).
- ⁹D. J. Fields, W. G. Lynch, C. B. Chitwood, C. K. Gelbke, M. B. Tsang, H. Utsunomiya, and J. Aichelin, *Phys. Rev. C* **30**, 1912 (1984).
- ¹⁰R. A. Loveman, *Phys. Rev. C* **33**, 2209 (1986).
- ¹¹H. R. Jaqaman, A. Z. Mekjian, and L. Zamick, *Phys. Rev. C* **29**, 2067 (1984).
- ¹²L. P. Csernai, G. Fai, and J. Randrup, *Phys. Lett.* **140B**, 149 (1984).
- ¹³S. Ben-Hao and D. H. E. Gross, *Nucl. Phys.* **A437**, 643 (1985).
- ¹⁴G. E. Beauvais and D. H. Boal, *Phys. Rev. C* (in press).
- ¹⁵P. Bonche, S. Levit, and D. Vautherin, *Nucl. Phys.* **A436**, 265 (1985).
- ¹⁶S. Levit and P. Bonche, *Nucl. Phys.* **A437**, 426 (1985).
- ¹⁷G. D. Westfall, B. V. Jacak, N. Anantaraman, M. W. Curtin, G. M. Crawley, C. K. Gelbke, B. Hasselquist, W. G. Lynch, D. K. Scott, M. B. Tsang, M. J. Murphy, T. J. M. Symons, R. Legrain, and T. J. Majors, *Phys. Lett.* **116B**, 118 (1982).
- ¹⁸B. V. Jacak, G. D. Westfall, C. K. Gelbke, L. H. Harwood, W. G. Lynch, D. K. Scott, H. Stöcker, and M. B. Tsang, *Phys. Rev. Lett.* **51**, 1846 (1983).
- ¹⁹J. P. Bondorf, S. I. A. Garpman, and J. Zimanyi, *Nucl. Phys.* **A296**, 320 (1978).
- ²⁰P. J. Siemens and J. O. Rasmussen, *Phys. Rev. Lett.* **42**, 880 (1979).
- ²¹H. Stöcker, A. A. Ogloblin, and W. Greiner, *Z. Phys. A* **303**, 259 (1981).
- ²²W. A. Friedman and W. G. Lynch, *Phys. Rev. C* **28**, 16 (1983).
- ²³A. S. Hirsch, A. Bujak, J. E. Finn, L. J. Gutay, R. W. Minich, N. T. Porile, R. P. Scharenberg, B. C. Stringfellow, and F. Turkot, *Phys. Rev. C* **29**, 508 (1984).
- ²⁴D. H. Boal, *Phys. Rev. C* **30**, 119 (1984).
- ²⁵H. Machner, *Phys. Rev. C* **31**, 1271 (1985).
- ²⁶D. J. Morrissey, W. Benenson, E. Kashy, B. Sherril, A. D. Panagiotou, R. A. Blue, R. M. Ronningen, J. van der Plicht, and H. Utsunomiya, *Phys. Lett.* **148B**, 423 (1984).
- ²⁷J. Pochodzalla, W. A. Friedman, C. K. Gelbke, W. G. Lynch, M. Maier, D. Ardouin, H. Delagrange, H. Doubre, C. Grégoire, A. Kyanowski, W. Mittig, A. Péghaire, J. Péter, F. Saint-Laurent, Y. P. Viyogi, B. Zwieglinski, G. Bizard, F. Lefèbvres, B. Tamain, and J. Québert, *Phys. Rev. Lett.* **55**, 177 (1985).
- ²⁸D. J. Morrissey, W. Benenson, E. Kashy, C. Bloch, M. Lowe, R. A. Blue, R. M. Ronningen, B. Sherrill, H. Utsunomiya, and I. Kelson, *Phys. Rev. C* **32**, 877 (1985).
- ²⁹J. Pochodzalla, W. A. Friedman, C. K. Gelbke, W. G. Lynch, M. Maier, D. Ardouin, H. Delagrange, H. Doubre, C. Grégoire, A. Kyanowski, W. Mittig, A. Péghaire, J. Péter, F. Saint-Laurent, Y. P. Viyogi, B. Zwieglinski, G. Bizard, F. Lefèbvres, B. Tamain, and J. Québert, *Phys. Lett.* **161B**, 275 (1985).
- ³⁰A. Z. Mekjian, *Phys. Rev. C* **17**, 1051 (1978).
- ³¹C. K. Gelbke, *Nucl. Phys.* **A400**, 473c (1983).
- ³²H. Stöcker, *J. Phys. G* **10**, L111 (1984).
- ³³M. A. Bernstein, W. A. Friedman, and W. G. Lynch, *Phys. Rev. C* **29**, 132 (1984).
- ³⁴H. W. Barz, J. P. Bondorf, R. Donangelo, I. N. Mishustin, and H. Schulz, *Nucl. Phys.* **A448**, 753 (1986).
- ³⁵D. H. Boal, *Phys. Rev. C* **30**, 749 (1984).
- ³⁶H. M. Xu, D. J. Fields, W. G. Lynch, M. B. Tsang, C. K. Gelbke, D. Hahn, M. R. Maier, D. J. Morrissey, J. Pochodzalla, H. Stöcker, D. G. Sarantites, L. G. Sobotka, M. L. Halbert, and D. C. Hensley, *Phys. Lett.* **182B**, 155 (1986).
- ³⁷R. Hanbury Brown and R. Q. Twiss, *Nature (London)* **178**, 1046 (1956).
- ³⁸G. I. Kopylov, *Phys. Lett.* **50B**, 472 (1974).
- ³⁹F. B. Yano and S. E. Koonin, *Phys. Lett.* **78B**, 556 (1978).
- ⁴⁰S. E. Koonin, *Phys. Lett.* **70B**, 43 (1977).
- ⁴¹H. Sato and K. Yazaki, in *High-Energy Nuclear Interactions and Properties of Dense Nuclear Matter*, edited by K. Nakai and A. S. Goldhaber (Hayashi-Kobo, Tokyo, 1980), p. 340.
- ⁴²B. K. Jennings, D. H. Boal, and J. C. Shillcock, *Phys. Rev. C* **33**, 1303 (1986).
- ⁴³W. G. Lynch, C. B. Chitwood, M. B. Tsang, D. J. Fields, D. R. Klesch, C. K. Gelbke, G. R. Young, T. C. Awes, R. L. Ferguson, F. E. Obenshain, F. Plasil, R. L. Robinson, and A. D. Panagiotou, *Phys. Rev. Lett.* **51**, 1850 (1983).
- ⁴⁴H. A. Gustafsson, H. H. Gutbrod, B. Kolb, H. Löhner, B. Ludewigt, A. M. Poskanzer, T. Renner, H. Riedesel, H. G. Ritter, A. Warwick, F. Weik, and H. Wieman, *Phys. Rev. Lett.* **53**, 544 (1984).
- ⁴⁵J. Pochodzalla, C. B. Chitwood, D. J. Fields, C. K. Gelbke, W. G. Lynch, M. B. Tsang, D. H. Boal, and J. C. Shillcock, *Phys. Lett.* **174B**, 36 (1986).
- ⁴⁶C. B. Chitwood, J. Aichelin, D. H. Boal, G. Bertsch, D. J. Fields, C. K. Gelbke, W. G. Lynch, M. B. Tsang, J. C. Shillcock, T. C. Awes, R. L. Ferguson, F. E. Obenshain, F. Plasil, R. L. Robinson, and G. R. Young, *Phys. Rev. Lett.* **54**, 302 (1985).
- ⁴⁷D. H. Boal and J. C. Shillcock, *Phys. Rev. C* **33**, 549 (1986).
- ⁴⁸C. B. Chitwood, C. K. Gelbke, J. Pochodzalla, Z. Chen, D. J. Fields, W. G. Lynch, R. Morse, M. B. Tsang, D. H. Boal, and J. C. Shillcock, *Phys. Lett.* **172B**, 27 (1986).
- ⁴⁹M. Gyulassy, *Phys. Rev. Lett.* **48**, 454 (1982).
- ⁵⁰S. Pratt, *Phys. Rev. Lett.* **53**, 1219 (1984).
- ⁵¹M. A. Bernstein and W. A. Friedman, *Phys. Rev. C* **31**, 843 (1985).
- ⁵²J. Pochodzalla, W. A. Friedman, C. K. Gelbke, W. G. Lynch, M. Maier, D. Ardouin, H. Delagrange, H. Doubre, C. Grégoire, A. Kyanowski, W. Mittig, A. Péghaire, J. Péter, F. Saint-Laurent, Y. P. Viyogi, B. Zwieglinski, G. Bizard, F. Lefèbvres, B. Tamain, and J. Québert, *Phys. Lett.* **161B**, 256 (1985).
- ⁵³D. H. Boal, *Phys. Rev. C* **29**, 967 (1984).
- ⁵⁴G. Bizard, A. Drouet, F. Lefèbvres, J. P. Patry, B. Tamain, F. Guilbault, and C. Lebrun, *Nucl. Instrum. Methods A* **244**, 483 (1986).
- ⁵⁵D. Ardouin, H. Delagrange, H. Doubre, C. Grégoire, A. Kyanowski, W. Mittig, A. Péghaire, J. Péter, F. Saint-Laurent, Y. P. Viyogi, B. Zwieglinski, J. Pochodzalla, C. K. Gelbke, W. Lynch, M. Maier, G. Bizard, F. Lefèbvres, B. Tamain, and J. Québert, *Nucl. Phys.* **A447**, 585c (1985), and unpublished.
- ⁵⁶A. Kyanowski, F. Saint-Laurent, D. Ardouin, H. Delagrange, H. Doubre, C. Grégoire, W. Mittig, A. Péghaire, J. Péter, Y. P. Viyogi, B. Zwieglinski, J. Québert, G. Bizard, F. Lefèbvres, B. Tamain, J. Pochodzalla, C. K. Gelbke, W. G. Lynch, and M. Maier, *Phys. Lett.* **181B**, 43 (1986), and unpublished.
- ⁵⁷C. J. Taylor, W. K. Jentschke, M. E. Remley, F. S. Eby, and P. G. Kruger, *Phys. Rev.* **84**, 1034 (1951); A. Meyer and R. B. Murray, *IEEE Trans. Nucl. Sci.* **NS-7**, 22 (1960).
- ⁵⁸T. C. Awes, G. Poggi, S. Saini, C. K. Gelbke, R. Legrain, and G. D. Westfall, *Phys. Lett.* **103B**, 417 (1981).
- ⁵⁹A. M. Poskanzer, G. W. Butler, and E. K. Hyde, *Phys. Rev. C* **3**, 882 (1971).
- ⁶⁰D. J. Fields, W. G. Lynch, T. K. Nayak, M. B. Tsang, C. B.

- Chitwood, R. Morse, C. K. Gelbke, J. Wilczynski, T. C. Awes, R. L. Ferguson, F. Plasil, F. E. Obenshain, and G. R. Young, *Phys. Rev. C* **34**, 536 (1986).
- ⁶¹L. D. Landau and E. M. Lifshitz, *Course of Theoretical Physics: Statistical Mechanics* (Pergamon, New York, 1980), Vol. 5, Pt. 1, pp. 236ff.
- ⁶²M. A. Bernstein, W. A. Friedman, W. G. Lynch, C. B. Chitwood, D. J. Fields, C. K. Gelbke, M. B. Tsang, T. C. Awes, R. L. Ferguson, F. E. Obenshain, F. Plasil, R. L. Robinson, and G. R. Young, *Phys. Rev. Lett.* **54**, 402 (1985).
- ⁶³S. Fiarman and W. E. Meyerhof, *Nucl. Phys.* **A206**, 1 (1973).
- ⁶⁴I. Y. Barit and V. A. Sergeev, *Yad. Fiz.* **13**, 1230 (1971) [*Sov. J. Nucl. Phys.* **13**, 708 (1971)].
- ⁶⁵F. Ajzenberg-Selove, *Nucl. Phys.* **A413**, 1 (1984); **A433**, 1 (1986); **A449**, 1 (1986).
- ⁶⁶J. Cerny, C. Detraz, and R. H. Pehl, *Phys. Rev. Lett.* **15**, 300 (1965).
- ⁶⁷T. A. Tombrello, *Phys. Rev.* **138**, B40 (1965).
- ⁶⁸H. D. Knox and R. O. Lane, *Nucl. Phys.* **A403**, 205 (1983).
- ⁶⁹N. Kumar, *Nucl. Phys.* **A410**, 50 (1983).
- ⁷⁰P. R. Christensen and C. L. Cocke, *Nucl. Phys.* **89**, 656 (1966).
- ⁷¹F. C. Barker and P. B. Treacy, *Nucl. Phys.* **38**, 33 (1962).
- ⁷²E. H. Berkowitz, G. L. Marolt, A. A. Rollefson, and C. P. Browne, *Phys. Rev. C* **4**, 1564 (1971).
- ⁷³F. D. Becchetti, C. A. Fields, R. S. Raymond, H. C. Bhang, and D. Overway, *Phys. Rev. C* **24**, 2401 (1981).
- ⁷⁴J. Pochodzalla, C. K. Gelbke, C. B. Chitwood, D. J. Fields, W. G. Lynch, M. B. Tsang, and W. A. Friedman, *Phys. Lett.* **175B**, 275 (1986).
- ⁷⁵B. A. Brown, C. R. Bronk, and P. E. Hodgson, *J. Phys. G* **10**, 1683 (1984).
- ⁷⁶Z. Chen, C. K. Gelbke, J. Pochodzalla, C. B. Chitwood, D. J. Fields, W. G. Lynch, and M. B. Tsang, *Phys. Lett. B* (in press).
- ⁷⁷Th. Stambach and R. L. Walter, *Nucl. Phys.* **A180**, 225 (1972).
- ⁷⁸W. Bretfeld, W. Burgmer, H. Eichner, D. Gola, Ch. Heinrich, H. J. Helten, H. Kretzer, K. Prescher, and W. Schnorrenberg, *Z. Phys. A* **282**, 365 (1977).
- ⁷⁹A. M. Lane and R. G. Thomas, *Rev. Mod. Phys.* **30**, 257 (1958).
- ⁸⁰D. Hahn and H. Stöcker, Lawrence Berkeley Laboratory Report LBL-22378, 1986, unpublished.
- ⁸¹H. D. Knox and R. O. Lane, *Nucl. Phys.* **A359**, 131 (1981).
- ⁸²G. J. Wozniak, N. A. Jelley, and J. Cerny, *Nucl. Instrum. Methods* **120**, 29 (1974).
- ⁸³H. W. Newson, R. M. Williamson, K. W. Jones, J. H. Gibbons, and H. Marshak, *Phys. Rev.* **108**, 1294 (1957).
- ⁸⁴R. Brockmann, J. W. Harris, A. Sandoval, R. Stock, H. Ströbele, G. Odyniex, H. G. Pugh, L. S. Schroeder, R. E. Renfordt, D. Schall, D. Bangert, W. Rauch, and K. L. Wolf, *Phys. Rev. Lett.* **53**, 2012 (1984).
- ⁸⁵A. Z. Mekjian, *Phys. Rev. Lett.* **38**, 640 (1977).
- ⁸⁶L. P. Csernai, H. Stöcker, P. R. Subramanian, G. Buchwald, G. Graebner, A. Rosenhauer, J. A. Muruhn, and W. Greiner, *Phys. Rev. C* **28**, 2001 (1983).
- ⁸⁷B. V. Jacak, H. Stöcker, and G. D. Westfall, *Phys. Rev. C* **29**, 1744 (1984).
- ⁸⁸J. Kapusta, *Phys. Rev. C* **24**, 2545 (1981).
- ⁸⁹G. Bertsch and P. J. Siemens, *Phys. Lett.* **126B**, 9 (1983).
- ⁹⁰J. A. Lopez and P. J. Siemens, *Nucl. Phys.* **A431**, 728 (1984).
- ⁹¹D. H. Boal and A. L. Goodman, *Phys. Rev. C* **33**, 1690 (1986).
- ⁹²D. J. Hinde, R. J. Charity, G. S. Foote, J. R. Leigh, J. O. Newton, S. Ogaza, and A. Chatterjee, *Phys. Rev. Lett.* **52**, 986 (1984).
- ⁹³W. P. Zank, D. Hilscher, G. Ingold, U. Jahnke, M. Lehmann, and H. Rossner, *Phys. Rev. C* **33**, 519 (1986).
- ⁹⁴D. H. Boal and H. DeGuise, *Phys. Rev. Lett.* **57**, 2901 (1986).
- ⁹⁵B. Borderie and M. F. Rivet, *Z. Phys. A* **321**, 703 (1985).
- ⁹⁶G. Auger, E. Plagnol, D. Jouan, C. Guet, D. Heuer, M. Maurel, H. Nifenecker, C. Ristori, F. Schussler, H. Doubre, and C. Grégoire, *Phys. Lett.* **169B**, 161 (1986).